Remote Sensing of Environment 311 (2024) 114269

Contents lists available at ScienceDirect

Remote Sensing of Environment

journal homepage: www.elsevier.com/locate/rse

# Not just a pretty picture: Mapping Leaf Area Index at 10 m resolution using Sentinel-2

Richard Fernandes [a,*], Gang Hong [a], Luke A. Brown [b], Jadu Dash [c], Kate Harvey [a], Simha Kalimipalli [a], Camryn MacDougall [a], Courtney Meier [d], Harry Morris [e], Hemit Shah [a], Abhay Sharma [a], Lixin Sun [a]

[a] Canada Centre for Remote Sensing, Natural Resources Canada, 580 Booth Street, Ottawa, Ontario K1A 0E4, Canada
[b] School of Science, Engineering & Environment, University of Salford, Manchester, M5 4WT, United Kingdom
[c] School of Geography and Environmental Science, University of Southampton, Highfield, Southampton SO17 1BJ, United Kingdom
[d] National Ecological Observatory Network, Battelle, Boulder, CO 80301, United States
[e] Climate and Earth Observation Group, National Physical Laboratory, Teddington TW11 0LW, United Kingdom

ARTICLE INFO

Editor Name: Jing M. Chen

*Keywords:*
Sentinel-2
Leaf area index
Downscaling
Validation

ABSTRACT

Achieving the Global Climate Observing System goal of 10 m resolution leaf area index (LAI) maps is critical for applications related to climate adaptation, sustainable agriculture, and ecosystem monitoring. Five strategies for producing 10 m LAI maps from Sentinel-2 (S2) imagery are evaluated: i. bi-cubic interpolation of 20 m resolution S2 LAI maps from the Simplified Level 2 Prototype Processor Version 1 (SL2PV1) as currently performed by the Sentinel Applications Platform (SNAP), ii. applying SL2PV1 to S2 reflectance bands spatially downscaled to 10 m using bi-cubic interpolation (BICUBIC), iii. Applying SL2PV1 to S2 reflectance bands spatially downscaled to 10 m using Area to Point Regression Kriging (ATPRK), iv. using a recalibrated version of SL2PV1 (SL2PV2) requiring only three S2 10m bands, and iv) a novel use of the previously developed Active Learning Regularization (ALR) approach to locally approximate the SL2PV1 algorithm using only 10 m bands.

Algorithms were assessed in terms of per-pixel accuracy and spatial metrics when comparing 10 m LAI maps produced using either actual S2 imagery or S2 imagery synthesized from airborne hyperspectral imagery to reference 10 m LAI maps traceable to in-situ fiducial reference measurements at 10 sites across the continental US. ATPRK and ALR algorithms had the lowest precision error of ~0.15 LAI, compared to 0.19 LAI for SNAP and BICUBIC and 0.35 LAI for SL2PV2, and ranked highest in terms of local correlation and Structural Similarity Index measure as well as qualitative agreement with reference maps. SL2PV2 LAI showed evidence of saturation over forests related to decreased sensitivity of input visible reflectance. All algorithms had a similar uncertainty of ~0.55 LAI compared to traceable reference maps, due to the trade-off between bias and precision. However, ATPRK and ALR uncertainty reduced to 0.11 LAI and 0.16 LAI, respectively, when compared to reference maps that ignored canopy clumping. These results suggest that both ATPRK and ALR are suitable for producing 10 m S2 LAI maps assuming bias due to local clumping can be corrected in the underlying SL2PV1 algorithm.

## 1. Introduction

Leaf area index (LAI) is an essential climate variable required by regional and global land surface models and for local climate adaptation and agricultural monitoring applications (WMO, 2022; Table 1). LAI can be systematically mapped at between 20 m and 30 m resolution using algorithms calibrated with radiative transfer models, and input data from imagers on Landsat and Sentinel-2 (S2) satellites (Ganguly et al., 2012; Kang et al., 2021; Weiss and Baret, 2016, hereafter WB2016; Weiss and Baret, 2020, hereafter WB2020; Brown et al., 2021a; Estevez et al., 2022; Fernandes et al., 2023). These algorithms satisfy the Global Climate Observing System (GCOS) baseline 100 m resolution requirement, but not the goal 10 m resolution requirement. Achieving 10 m resolution is critical for applications such as monitoring ecological recovery of reclaimed well sites (Lupardus et al., 2019), quantifying urban ecosystem vegetation cover (Tran et al., 2011), monitoring crop growth

* Corresponding author.
*E-mail address:* Richard.Fernandes@canada.ca (R. Fernandes).

https://doi.org/10.1016/j.rse.2024.114269
Received 21 February 2024; Received in revised form 9 May 2024; Accepted 12 June 2024
Available online 28 June 2024

**Table 1**
GCOS goal (G), baseline (B) and threshold (T) LAI requirements.

| Definition | one half of the total green leaf area per unit horizontal ground area | | |
|---|---|---|---|
| Unit | $m^2m^{-2}$ | | |
| Requirement | Unit | Metric | Value |
| Horizontal Resolution | m | G | 10 |
| | | B | 100 |
| | | T | 250 |
| Temporal Resolution | days | G | 1 |
| | | B | – |
| | | T | 10 |
| Timeliness | days | G | 1 |
| | | B | 5 |
| | | T | 10 |
| Required measurement uncertainty | % or $m^2m^{-2}$ | G | max(10%, 0.5) |
| | | B | – |
| | | T | max(20%, 0.5) |
| Stability | $m^2m^{-2}$ /decade | G | 3% |
| | | B | – |
| | | T | 6% |

and yield (Mulla, 2013; Yang et al., 2009; Defourny et al., 2019) and modelling water use (McCabe et al., 2017). Increasing resolution could also potentially reduce thematic uncertainty due to mixed pixels (Tian et al., 2001; Fernandes et al., 2003; Garrigues et al., 2006; Jin et al., 2007; Fang et al., 2013; Xu et al., 2020; Dong et al., 2023).

The Simplified Level 2 Prototype Processor Version 2 (SL2PV2) algorithm (WB2020) maps LAI at 10 m resolution using surface bi-directional reflectance (ρ) from three 10 m S2 Multispectral Instrument spectral bands (Table 2). SL2PV2 is a simplification of the Simplified Level 2 Prototype Processor Version 1 (SL2PV1) algorithm (WB2016) that uses eight S2 bands aggregated to 20 m resolution (Table 2). SL2PV1 LAI meets GCOS uncertainty requirements ~92% of the time over non-forested sites (Djamai et al., 2019; Brown et al., 2021a) and, once a bias correction to account for canopy clumping is applied, ~55% of the time for forest sites (Fernandes et al., 2023). Cross-validation using spatially homogeneous radiative transfer model simulations indicates that SL2PV2 and SL2PV1 LAI agree within ±0.5 LAI (50 percentile), with SL2PV2 overestimating SL2PV1 LAI by ~10% for LAI > 4 (WB2020). However, SL2PV2 has yet to be validated against reference maps traceable to in-situ reference measurements (RM), as recommended by good practice (Fernandes et al., 2014).

SL2PV2 uses a single, land cover independent, regression to estimate LAI. In principle, higher resolution LAI maps could also be generated using regression estimators calibrated locally with LAI products and matching upscaled high resolution bands, and then applied to original high-resolution imagery (Houborg and McCabe, 2018; Kimm et al., 2020; Kang et al., 2021). For example, the Active Learning Regularization (ALR) algorithm (Djamai and Fernandes, 2021) calibrates a local LAI regression estimator, given a dictionary of candidate regressors, by using matchups between vegetation indices (VIs) derived from SL2PV2 input bands aggregated to 20 m resolution and their corresponding 20 m SL2PV1 LAI. In doing so, ALR incorporates the information useful for LAI retrieval contained in all S2 bands using a local approximation using only the 10 m bands. Here, ALR is used to produce 10 m resolution S2 LAI maps by only using VIs derived from 10 m S2 bands.

Spatial interpolation of coarser resolution LAI maps can also produce 10 m resolution S2 LAI maps. The European Space Agency (ESA) Sentinel Applications Package implements bi-cubic interpolation of 20 m resolution SL2PV1 LAI maps to generate 10 m resolution maps (SNAP, SNAP - ESA Sentinel Application Platform v9.0.0, http://step.esa.int accessed on August 25, 2023). However, spatial interpolation may increase thematic uncertainty due to the non-linear relationship between ρ and LAI (Tian et al., 2001).

Instead of spatial interpolation of LAI maps, SL2PV1 could also be applied to the original 10 m S2 bands and 20 m S2 bands spatially interpolated or downscaled to 10 m resolution. Radiance scales as a linear function of the sensor point spread function (Schowengerdt, 2012) so downscaling reflectance scaling may be result in lower overall uncertainty than attempting to downscale LAI products, that are in general non-linear function of reflectance (Tian et al., 2001). Spatial downscaling algorithms have been validated in terms of estimating 10 m resolution ρ from S2 (Park et al., 2019; Armannsson et al., 2021), and in terms of the accuracy of downstream 10 m resolution land cover classification maps (Zheng et al., 2017; Xu and Somers, 2021), but not in terms of estimating 10 m resolution LAI maps using S2. Here, SL2PV1 combined with Area to Point Regression Kriging (ATPRK, Wang et al., 2016a and Wang et al., 2016b) spatial downscaling is evaluated in terms of 10 m LAI estimation. ATPRK was chosen from the many available spatial downscaling algorithms as it resulted in the lowest uncertainty, amongst state-of-the-art method, when downscaling S2 reflectance (Armannsson et al., 2021). Bi-cubic spline interpolation of 20 m reflectance inputs followed by application of SL2PV1 (BICUBIC) was also tested as it could be applied to sensors such as the Landsat Operation Line Imager that do not have 10 m bands.

The goal of our study was to validate SL2PV2, ALR, SNAP, ATPRK, and BICUBIC algorithms for producing 10 m resolution S2 LAI maps. Following good practice (Fernandes et al., 2014), validation was performed by comparing 10 m LAI maps, generated by applying each algorithm to both actual and synthetic S2 imagery, to reference 10 m resolution LAI maps traceable to in-situ reference RM (REFRM). Accuracy (A), precision (P), uncertainty (U) and spatial similarity metrics were quantified for ten different study sites across the continental United States of America (US). The metrics were summarized for each site and, since the purpose of downscaling is not simply to reduce thematic uncertainty but also to improve the realism of the spatial pattern of the LAI map, also as a function of local coefficient of variation of reference LAI maps.

We hypothesized that SNAP would result in the worst spatial similarity metrics as it does not account for the non-linear relationship

**Table 2**
Sentinel-2A spectral bands used for SL2V1 (bold font) and SL2PV2 (10 m resolution) algorithms. FWHM corresponds to Full Width Half Maximum, ACT corresponds to across track, ALT corresponds to along track and Ref corresponds to reference band.

| Band | Centre Wavelength | Bandwidth | Resolution | Modulation Transfer Function | | Mis-registration |
|---|---|---|---|---|---|---|
| | nm | FWHM nm | Gridded m | FWHM ACT cycles/pixel | FWHM ALT cycles/pixel | 3sigma m |
| **B03** | **559.8** | **36** | **10** | **0.27** | **0.28** | **2.4** |
| **B04** | **664.6** | **31** | **10** | **0.35** | **0.23** | **3.5** |
| **B05** | **704.1** | **15** | **20** | **0.42** | **0.34** | **Ref** |
| **B06** | **740.5** | **15** | **20** | **0.35** | **0.33** | **2.4** |
| **B07** | **782.8** | **20** | **20** | **0.35** | **0.34** | **2.8** |
| B8 | 832.8 | 106 | 10 | 0.26 | 0.25 | 2.5 |
| **B8A** | **864.7** | **21** | **20** | **0.36** | **0.31** | **3.8** |
| **B11** | **1613.7** | **91** | **20** | **0.20** | **0.24** | **5.4** |
| **B12** | **2202.4** | **175** | **20** | **0.24** | **0.22** | **5.2** |

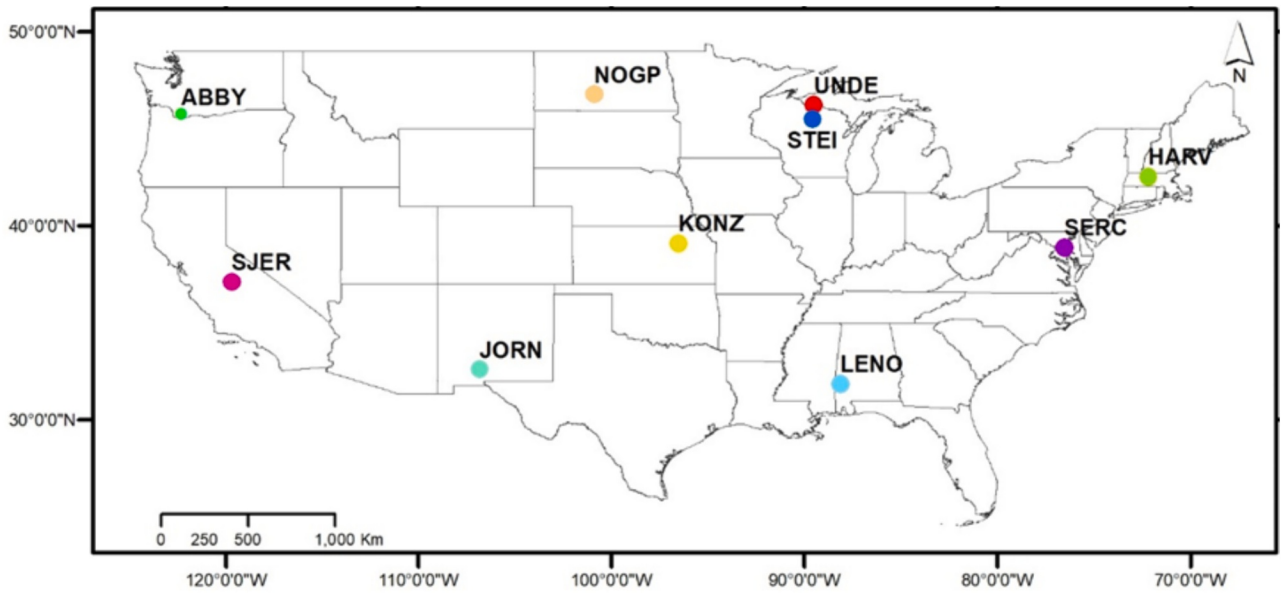


**Fig. 1.** Study site locations.

**Table 3**
NEON study site descriptions (https://www.neonscience.org/field-sites/explore-field-sites) together with AHS and S2 dates. Land cover corresponds to NEON legend: Evergreen Forest (EF), Mixed Forest (MF), Deciduous Forest(DF), Woody Wetlands (WF), Shrub Scrub (SH), Cultivated Crops (CR), Grassland Herbaceous (GR). #ESU correspond to the maximum number of unique elementary sampling units over all dates surveyed at a site.

| Site | Name | Land Cover | Lat. °N | Long. °W | Elev. m. a.s.l. | AHS Date | S2 Date | #ESU | LAI Min. | LAI Max. |
|---|---|---|---|---|---|---|---|---|---|---|
| ABBY | Abby Road | EF/SH | 45.762 | 122.330 | 365 | 2021-07-19 | 2021-07-19 | 18 | 1.11 | 7.62 |
| HARV | Harvard Forest | EF/MF | 42.536 | 72.172 | 341 | 2019-08-26 | 2019-08-26 | 21 | 0.36 | 6.74 |
| JORN | Jornada Experimental Range | SH | 32.591 | 106.843 | 1324 | 2019-08-25 | 2019-08-25 | 23 | 0.01 | 0.22 |
| KONZ | Konza Prairie Biological Station | DF/GR | 38.946 | 96.443 | 396 | 2020-07-13 | 2020-07-13 | 23 | 0.01 | 5.76 |
| LENO | Lenoir Landing | DF/WF | 31.854 | 88.161 | 13 | 2021-04-22 | 2021-04-22 | 24 | 0.17 | 6.87 |
| NOGP | Northern Great Plains Laboratory | GR | 46.770 | 100.915 | 589 | 2020-06-26 | 2020-06-27 | 23 | 0.01 | 2.2 |
| SERC | Smithsonian Environmental Research Center | CR/DF | 38.890 | 76.560 | 33 | 2021-08-11 | 2021-08-10 | 25 | 0.01 | 7.38 |
| SJER | San Joaquin Experimental Range | EF/SH | 37.109 | 119.732 | 400 | 2021-03-31 | 2021-04-01 | 23 | 0.01 | 4.43 |
| STEI | Steigerwaldt-Chequamegon | DF/MF/WF | 45.509 | 89.586 | 476 | 2019-06-08 | 2019-06-08 | 23 | 0.63 | 7.21 |
| UNDE | University of Notre Dame Environmental Center | DF/MF/WF | 46.234 | 89.537 | 521 | 2019-06-06 | 2019-06-06 | 27 | 0.44 | 6.23 |

between LAI and ρ. In contrast, we hypothesized that ALR and SL2PV2 would have the best spatial metrics as they directly employ the 10 m S2 bands without applying spatial operators to infer 10 m patterns from 20 m bands. We also hypothesized that ATPRK would perform best in terms of A, P and U metrics as, unlike SNAP, it avoids averaging over non-linear relationships, and, unlike ALR and SL2PV2, it uses additional input bands shown to improve LAI retrieval in comparison to the 10 m S2 bands alone (Verger et al., 2011).

Our study is the first to quantify the impact of spatial downscaling of reflectance on LAI product uncertainty using high resolution reference images traceable to in-situ fiducial reference measurements. This is critical since SL2P relies on the covariation of input bands in a non-linear manner that may not be reflected by simply propagating the uncertainty of downscaled ρ. Our study is also the first to compare the thematic performance of widely used SL2PV1 and SNAP approaches with locally calibrated approaches such as ALR and ATPRK. In fact, the use of ALR for downscaling is novel in itself. Finally, our study uses a sufficient range of sites to quantify the performance of each algorithm across different land cover. Understanding the thematic performance of these algorithms will enable users to determine if they are suitable of generating 10 m resolution LAI products and allow researchers and space agencies to prioritize the development and deployment of such algorithms.

## 2. Materials and methods

### 2.1. Materials

#### 2.1.1. NEON AHS imagery

Airborne hyperspectral sensor (AHS) 1 m pixel resolution surface reflectance (ρ) images, acquired at 10 National Ecological Observatory Network sites (NEON; Barnett et al., 2019; Fig. 1), were used to simulate synthetic S2 imagery and to produce 10 m resolution reference LAI maps. NEON sites were selected since representative in-situ LAI RM were available for a ~ 1.5 km × 1.5 km region around a meteorological tower at each site (Brown et al., 2020). Only acquisitions from 2019 onwards were used to match the availability of systematically processed S2 ρ imagery from ESA.

Metadata for all 3973 spectrometer orthorectified flightline ρ products covering the tower at each of the 47 terrestrial NEON sites were extracted from the NEON Data Portal (NEON, 2023a). Orthorectified ρ products corresponded to cloud, cloud shadow, and haze screened 1 m resolution ρ estimated by applying ATCOR4 to spectrometer orthorectified surface directional radiance flightline products (NEON, 2023b). Flights were timed to capture the peak greenness, determined from a 15-yr analysis of Moderate Resolution Imaging Spectroradiometer normalized difference vegetation index measurements. Flight lines between 5 km and 20 km along track were flown at ~1 km above ground

level and a groundspeed of ~185 km/h along a North-South track. At sensor radiance imagery was acquired using the 34° across track field of view, 1 mrad instantaneous field of view, NEON Imaging Spectrometer (https://www.neonscience.org/data-collection/imaging-spectrometer accessed on August 28, 2023); resulting in an ~600 m across track width, an ~0.5 m across track ground sampling distance, and an ~1 m along track ground sampling distance. Radiance was measured at 5 nm intervals between 380 nm and 2510 nm for 6 nm full width half maximum bands and resampled to 1 m resolution with a mean geolocation error of 0.23 m (Kampe and Gallery, 2015). AHS ρ uncertainty has not been published but it is likely lower than matching S2 L2A products given that AHS radiance is measured at ~1 km above ground level versus at the top of the atmosphere for S2.

AHS images satisfying the following criteria were retained for validation:

I. terrain with <6° slope, using the 90 arcsec MERIT digital elevation model (Yamazaki et al., 2017),
II. greater than 90% clear sky pixels for the AHS image,
III. a S2 acquisition within ±3 days with >90% clear sky pixels over the flight line,
IV. NEON tower site contained within the swath.

The terrain constraint ensured ATCOR4 adjacency correction was not applied given biases due to this correction previously observed with S2 imagery (Djamai and Fernandes, 2018). Images were co-located with tower sites since only sub-areas around tower sites for which in-situ RM were representative were used during validation. One retained AHS image was chosen at each of 10 NEON sites elected to span a range of ecozones and land cover conditions (Table 3, Fig. 1).

#### 2.1.2. S2 level 2A surface reflectance products

Cloud free Copernicus Sentinel-2 A and Sentinel-2B Level 2 A Collection 1 ρ products (L2) covering each retained AHS image within ±3 days were acquired from the Copernicus Open Access Hub accessed on October 20, 2023). L2 products were generated by the European Space Agency using the Sen2Cor algorithm, which uses a version of ATCOR4 (ATCOR) for atmospheric correction but differs from AHS processing in approaches to clear sky identification and the use of a global rather than a local aerosol model (Müller-Wilm, 2018). Sen2Cor maps clear sky pixels with 98% accuracy and estimates ρ with an uncertainty better than 0.005 + 0.05ρ for flat surfaces with uniform soil and vegetation cover (Doxani et al., 2018). Geolocation uncertainty is <12.5 m 95% circular error probable (Gascon et al., 2017). Band to band misregistration ranges from 2.4 m to 5.8 m at 3 standard deviations (Table 2; Clerc and MPC team, 2021). The full width half maximum of the across track modulation transfer function ranges from ~0.20 cycles/pixel for B11 to ~0.42 cycles/pixel, with moderate anisotropy present in B04, B05 and B11 (Table 2; Clerc and MPC team, 2021). Variation in the projected instantaneous field of view with view angle is far less than the pixel size as the field of view is only 20.6° (Gascon et al., 2017).

#### 2.1.3. In-situ LAI fiducial reference measurements

Representative in-situ LAI fiducial RM (in-situ RM) for NEON sites, from the Ground Based Observation for Validation component of the Copernicus Land Monitoring Service (https://land.copernicus.eu/global/gbov/ accessed on October 20, 2023), supplemented with identically acquired and processed in-situ NEON data by the authors, were used to calibrate reference LAI maps derived from AHS imagery. For each site, in-situ RM corresponded to the sum of overstory and understory LAI. LAI was estimated by multiplying indirect estimates of plant area index (PAI), defined as half the total vegetation surface area per unity horizontal area, by land cover specific conversion factors corresponding to the complement of the woody-to-total area ratio (Brown et al., 2021a). PAI was estimated separately by applying HemiPy (Brown et al., 2023) to 12 digital hemispherical photographs (DHPs) acquired facing upwards, for overstory, or downwards, for understory, at between 23 and 26 20 m × 20 m square elementary sampling units (ESUs) representative of land cover within ~5 km of the tower (NEON, 2023c). Validation using synthetic forest scenes indicates HemiPY tends to underestimate PAI by ~5% for LAI < 4 and no >10% in general (Brown et al., 2023). This bias was not corrected as it has not been quantified on a land cover specific basis. The effective PAI (PAIe), defined as the PAI required to match the negative logarithm of the azimuthal averaged gap fraction integrated over the upper hemisphere (Eq. 1 of Chen et al., 1997), was also estimated using HemiPy for each RM and subsequently converted to LAIe using the same factors applied to estimate LAI from PAI. Three ESU's adjacent to the NEON instrumented towers were sampled bi-weekly from leaf-out through senescence, with the remaining ESU's distributed across major NLCD classes at each NEON site and sampled every 5 years within a 1 month window that includes the AHS imagery. LAI, together with the one standard deviation uncertainty of estimates LAI and effective LAI (LAIe), were derived according to a fiducial RM protocol (Brown et al., 2021b).

### 2.2. Methods

#### 2.2.1. Synthetic image generation

A synthetic 10 m reference image with S2 bands (A10m) and a synthetic S2 A image with S2 spatial resolution (AL2) was produced from each AHS image by first generating an image of 1 m S2 equivalent spectral bands (A1m) and then spatial smoothing and sub-sampling the 1 m bands (AL2) as follows:

i. A1m: AHS imagery was interpolated to 1 nm spectral resolution using shape-preserving piecewise cubic splines (Mathworks, 2023), followed by convolution with Sentinel-2 A spectral response functions (ESA, 2023a) to produce spectral bands corresponding to S2 bands. This approach was deemed suitable since the combination of 5 nm sampling interval and 6.5 nm FWHM bandwidth results in a constant gain of 0.2 across all wavelengths between 383 nm and 2507 nm.
ii. A10m: A 10 m × 10 m moving average filter was applied to each A1m band followed by multiplication with a 10 m × 10 m spacing sampler to produce input for reference LAI maps with exactly 10 m grid spacing and 10 m spatial scale.
iii. AL2: Each A1m band was filtered using the S2A point spread function (ESA, 2023b). Filtered bands were then shifted by a vector randomly sampled from an isotropic Gaussian distribution with standard deviation determined by the nominal band-to-band misregistration error (Table 2) and then nearest neighbour subsampled to the A10 m grid. The 20 m resolution bands were then synthesized by applying a 20 m × 20 m subsampler aligned with the A10 m grid.

#### 2.2.2. S2 L2 post processing

L2 georeferencing was visually assessed by comparison to A1m images at 10 control points spread across the A1m image. L2 products meeting the nominal S2 georeferencing specification were radiometrically cross-calibrated to AL2 products to minimize differences in radiometric calibration and atmospheric correction. Cross-calibration was performed by applying site and band specific linear models to the L2 product. Each model was determined by Thiel-Sen regression calibrated using data from matching L2 and AL2 bands, both smoothed with a 60 m square moving average filter to minimize the impact of misregistration, and sub-sampled at the nominal centre of every sixth (third) row and column of the 10 m (20 m) bands.

#### 2.2.3. 10 m LAI product generation

L2 and AL2 products were clipped to the extent of their corresponding A10 m products, with edge pixels discarded from all images.

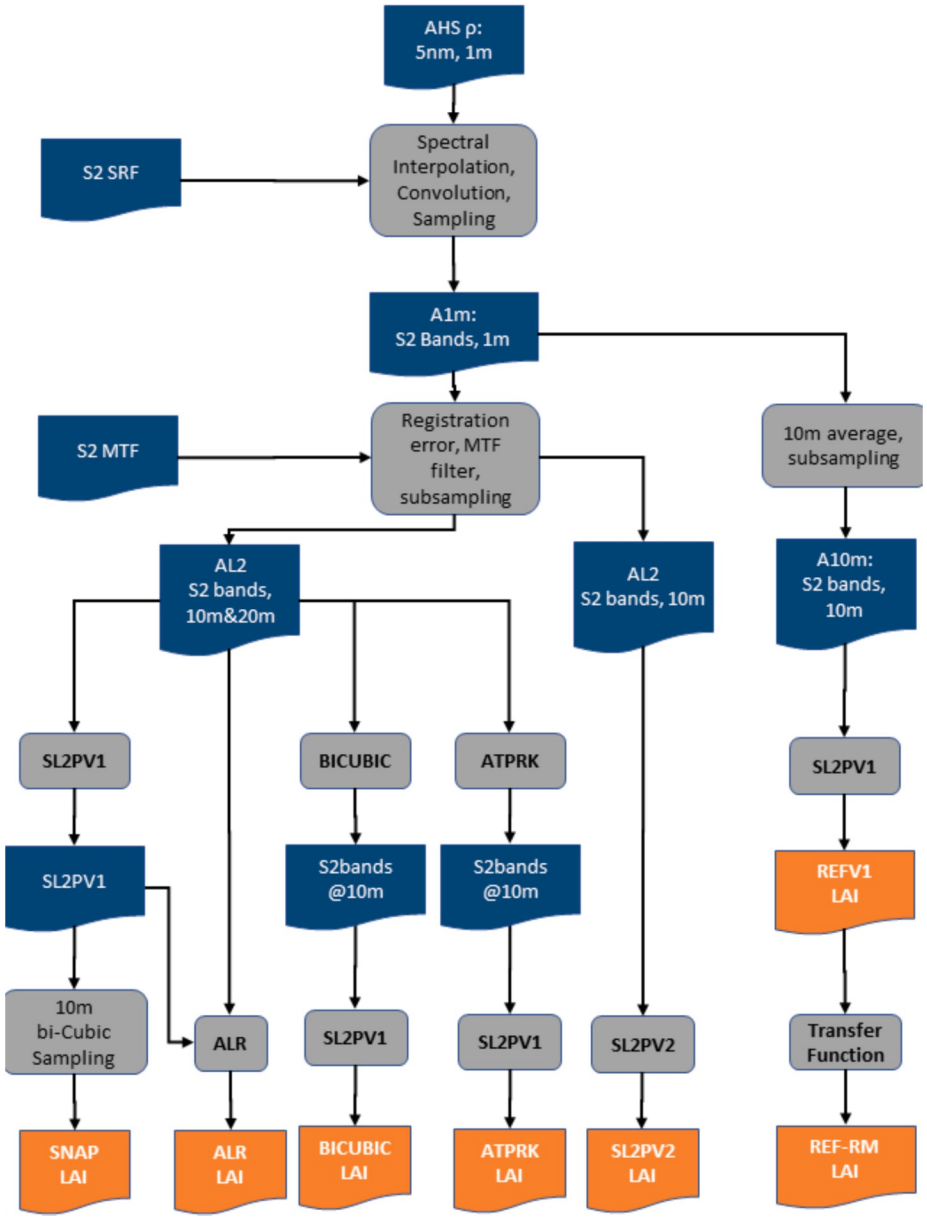


**Fig. 2.** LAI production flow chart from AHS imagery. Blue boxes indicate algorithm inputs. Gray boxes indicate algorithms. Orange boxes indicate LAI products. SRF corresponds to spectral response function. MTF corresponds to modulation transfer function. (For interpretation of the references to colour in this figure legend, the reader is referred to the web version of this article.)

Reference 10 m LAI maps were generated by apply SL2PV1 to the A10 m images and 10 m downscaled LAI maps were produced from both AL2 images (Fig. 2) and L2 images (Appendix B, Fig. B1) as described below. The Landscape Evolution and Forecasting Toolbox implementation of SL2PV1 and SL2PV2 (Fernandes et al., 2021), matching the algorithm theoretical basis document of WB2016 and WB2020, respectively, was used when generating 10 m products.

*2.2.3.1. Reference products.* Good practice requires traceability of reference LAI maps to in-situ RM (Fernandes et al., 2014). Typically, a LAI map traceable to RM (labelled here REFRM) is produced by applying a transfer function (TF) calibrated using representative co-located in-situ LAI RM and either ρ (Fernandes et al., 2014) or uncalibrated LAI products (Brown et al., 2020). Neither approach was possible here since the spatial footprint of the in-situ LAI RM exceeded the 10 m resolution of the desired reference maps (Fernandes et al., 2023). Instead, a three-step approach was used to calibrate site specific TFs applied to derive REFRM products.

The first step corresponds to generating a reference 10 m LAI map without traceability to in-situ RM (REFV1). As in Brown et al. (2020), SL2PV1 was used to generate this map, together with a quality layer indicating valid retrievals as described in Fernandes et al. (2023), for each A10 m product. REFV1 maps cannot be used for a traceable validation of downscaled products since SL2PV1 LAI is biased over the NEON sites as it does not account for canopy clumping (Brown et al., 2021a; Fernandes et al., 2023; Fernandes et al., 2024).

The second step corresponds to calibrating and applying a site-specific regression to convert REFV1 LAI to LAIe. This strategy is motivated by the fact that SL2PV1 already provides almost unbiased estimates of LAIe irrespective of land cover or location across the NEON sites (Brown et al., 2021a). The strategy was also simplified by the fact that the regression could be calibrated using an existing dataset of SL2PV1 LAI estimates from 20 m resolution S2 imagery matching in-situ LAIe RM, as well as associated 1 s uncertainty estimates (Brown et al.,

**Table 4**
Thematic performance metrics.

| Metric | Symbol | Definition |
|---|---|---|
| Uncertainty | U | Root mean square of estimates minus reference. |
| Accuracy | A | Mean of estimates minus reference. |
| Precision | P | Root mean square of estimates minus reference minus A. |
| Pearson correlation coefficient | R | Ratio of covariance of estimates and reference to product of their standard deviation. |
| Structural Similarity Index Measure | SSIM | Wang et al., 2004. |

2021a). In-situ LAIe RM were matched to SL2PV1 LAI using spatial footprints modelled based on canopy height (Brown et al., 2020). SL2PV1 1 s uncertainty estimates were decreased by 50% since they generally overestimate actual uncertainty (Brown et al., 2021a). Ideally, one would only use matches corresponding to the site of a fitted regression. However, the requirement of clear sky matchups resulted in imbalanced samples in terms of RM LAIe for many sites. To address this limitation, site specific regressions were fit using all NEON ESUs sharing the land cover of any ESUs within the site. The uncertainty due to this assumption was quantified using the regression 67.5 percentile confidence prediction interval (PI). Thiel-Sen regression was used to estimate in-situ RM LAIe as a function of SL2PV1 LAI as it is the only statistically consistent slope estimator in the presence of both unknown measurement errors and $< 28\%$ outliers (Fernandes and Leblanc, 2005). SL2PV1 LAI measurements were log transformed prior to the regression fit to account for multiplicative error associated with signal saturation at higher LAIe (Brown et al., 2021a).

The third step corresponds to calibrating and applying a site-specific scaling factor to convert the in-situ RM LAIe estimate from the second step to an estimate of in-situ RM LAI. The scaling factor was estimated as the slope of a zero-intercept Thiel-Sen regression using within-site measurements of in-situ LAI RM as response and corresponding in-situ LAIe as regressor. In this case, there were sufficient local measurements for a site-specific calibration. This step assumes that, for spatial footprints between $100m^2$ and $200m^2$, the ratio of LAIe to LAI, also known as the canopy clumping index (Chen et al., 1997), was constant across a given site; an assumption motivated by the fact that NEON site towers were located such that the landscape in the fetch of their instruments could be considered homogeneous in terms of spatial patterns of land cover and vegetation density (Barnett et al., 2019). The impact of this assumption on REFRM uncertainty was quantified using the regression PI(.

The product of the regression relating SL2PV1 LAI to in-situ LAIe and the scaling factor relating in-situ LAIe to in-situ LAI was then used as the site specific TF applied to the A10 m product of the site. The 67.5% PI for the TF estimate of LAI was modelled as the Euclidean sum of the PIs of both regressions. Negative LAI predictions were assigned a value of 0 but with the same uncertainty as the in-situ LAI prediction for the minimum observed SL2V1 LAI at the site.

*2.2.3.2. SNAP.* The 10 m bands of each AL2 and L2 product were aggregated to 20 m resolution using averaging of the four 10 m pixels falling within each nominal 20 m pixel. SL2PV1 was then applied to this result to generate a 20 m LAI product, along with a quality mask indicating valid clear sky retrievals. The Landscape Evolution and Forecasting Toolbox implementation of SL2PV1 (Fernandes et al., 2021), with neural networks consistent with the algorithm theoretical basis document of WB2016, was used. The 20 m LAI products were then interpolated to 10 m resolution pixels centered at the input product 10 m grid using the bi-cubic spline interpolation with the Geospatial Data Abstraction.

software Library gdal.WARP function (GDAL/OGR contributors, 2024), to produce a final SNAP 10 m LAI product.

*2.2.3.3. SL2PV2.* SL2PV2 was applied separately to the required 10 m input bands (Table 2) of each AL2 or L2 products to generate a 10 m LAI product, along with a quality mask indicating valid clear sky retrievals.

*2.2.3.4. ALR.* ALR is described in detail in Djamai and Fernandes (2018) and provided as open-source code (https://github.com/hongirsa/ALR accessed on October 30, 2023), so only information required to replicate results used in this study are provided here. The 10 m bands of each AL2 and L2 product were aggregated to 20 m resolution using averaging of the four 10 m pixels falling within each nominal 20 m pixel. A calibration dataset was produced by sampling these aggregated bands, augmented with a library of VIs derived from them (https://custom-scripts.sentinel-hub.com/custom-scripts/sentinel-2/indexdb/, accessed October 10, 2023), and matching valid SL2PV1 20 m LAI retrievals. A two-stage feature selection procedure was applied to select input bands or VIs used for prediction. First, only one feature from any set of inputs with pairwise correlation $>0.95$ was retained. Second, the first 5 non-zero coefficients of a 10 fold cross validated Least Angle Regression (https://scikit-learn.org/stable/modules/generated/sklearn.linear_model.LarsCV.html#sklearn.linear_model.LarsCV accessed on October 10, 2023) of LAI versus the retained features were selected as regressors. The revised calibration dataset was then trimmed by discarding samples corresponding to lowest 5 percentile and highest 95 percentile values of each regressor conditional on LAI. The Google Earth Engine implementation of random forest regression (https://developers.google.com/earth-engine/apidocs/ee-classifier-smilerandomforest accessed on October 10, 2023) with default settings of 100 trees, a minimum leaf node size of one, and a 0.5 bag fraction, was calibrated with the trimmed database to produce a local regression algorithm. The regression was then applied to the selected features produced using the original 10 m resolution bands in the input image to generate a 10 m resolution LAI map. A quality mask indicating valid clear sky retrieval was produced using the same approach as for SL2PV1 but based on the local calibration database rather than the original SL2PV1 calibration database.

*2.2.3.5. ATPRK.* ATPRK was applied to each AL2 or L2 product to produce 10 m resolution estimates of their 20 m resolution bands using a MATLAB implementation tuned for S2 (https://github.com/qunmingwang/Code-for-S2-fusion accessed on October 10, 2023). ATPRK predicts $\rho$ at the nominal center of a reference 10 m resolution band (here B04) as the sum of a band specific regression prediction calibrated on the entire image and an area to point kriging estimate of the regression residuals at 10 m resolution. The regression prediction first calibrates a multi-variate linear regression estimate of a given 20 m S2 band $\rho$ given the $\rho$ for the four 10 m S2 bands, upscaled to the 20 m band assuming a nominal S2 PSF. The calibrated regression is then applied to the original 10 m S2 bands to provide a regression prediction of the 20 m S2 band at 10 m resolution. A 10 m resolution residual image between the original 20 m S2 band and the 10 m regression prediction, is upscaled to 20 m using the nominal S2 PSF, subsampled to the nominal 20 m grid, and then interpolated to 10 m resolution using kriging; with semi-variograms estimated by spatial deconvolution of the semi variogram between 20 m residuals and all input bands upscaled to 20 m resolution. SL2PV1 was applied to both the downscaled 10 m resolution L2 and AL2 $\rho$ imagery to produce 10 m resolution LAI maps.

*2.2.3.6. BICUBIC.* The gdal.WARP function was used to convert 20 m resolution input bands to 10 m resolution reflectance bands reflectance. SL2PV1 was then applied to the resulting 10 m products to generate 10 m LAI products, along with a quality mask indicating valid clear sky retrievals.

*2.2.4. Thematic performance metrics*

Thematic performance metrics were derived using comparisons of

**Table 5**
Direct validation metrics for 20 m SL2PV1 maps (20 m SL2PV1) and regression statistics for transfer function (TF) calibration. N corresponds to number of samples and PI is the width of the 67.5 percentile prediction interval.

| Site | 20 m SL2PV1 | | | SL2PV1 LAI vs In-situ LAIe | | | | | | In-Situ LAIe vs In-Situ LAI | | | | | TF |
|---|---|---|---|---|---|---|---|---|---|---|---|---|---|---|---|
| | A | U | R2 | N | Slope | Int. | PI | U | R2 | N | Slope | PI | U | R2 | PI |
| **ABBY** | −0.4 | 0.61 | 0.66 | 253 | 2.04 | −0.53 | 0.50 | 0.24 | 0.66 | 211 | 1.55 | 0.45 | 0.21 | 0.96 | 0.67 |
| **HARV** | −1.17 | 1.31 | 0.32 | 253 | 2.04 | −0.53 | 0.50 | 0.24 | 0.66 | 378 | 1.34 | 0.36 | 0.12 | 0.94 | 0.61 |
| JORN | 0.2 | 0.20 | 0.27 | 214 | 0.36 | −0.06 | 0.09 | 0.02 | 0.28 | 335 | 1.04 | 0.01 | 0.00 | 0.92 | 0.09 |
| KONZ | −0.69 | 0.97 | 0.83 | 505 | 2.23 | −0.53 | 0.46 | 0.21 | 0.83 | 352 | 1.06 | 0.08 | 0.01 | 0.98 | 0.47 |
| LENO | −1.04 | 1.14 | 0.57 | 385 | 1.66 | 0.24 | 0.50 | 0.25 | 0.57 | 307 | 1.33 | 0.33 | 0.01 | 0.98 | 0.60 |
| NOGP | 0.07 | 0.31 | 0.63 | 168 | 1.40 | −0.31 | 0.39 | 0.08 | 0.64 | 274 | 1.05 | 0.05 | 0.00 | 0.99 | 0.30 |
| **SERC** | −0.9 | 1.07 | 0.75 | 412 | 2.04 | −0.27 | 0.51 | 0.25 | 0.74 | 362 | 1.36 | 0.42 | 0.17 | 0.91 | 0.66 |
| **SJER** | −0.4 | 0.61 | 0.66 | 253 | 2.04 | −0.53 | 0.50 | 0.24 | 0.66 | 342 | 1.53 | 0.37 | 0.12 | 0.97 | 0.62 |
| **STEI** | −1.34 | 1.46 | 0.46 | 455 | 1.73 | 0.20 | 0.53 | 0.27 | 0.54 | 265 | 1.36 | 0.44 | 0.19 | 0.92 | 0.69 |
| **UNDE** | −1.07 | 1.28 | 0.46 | 455 | 1.73 | 0.20 | 0.53 | 0.27 | 0.54 | 286 | 1.45 | 0.42 | 0.17 | 0.97 | 0.68 |

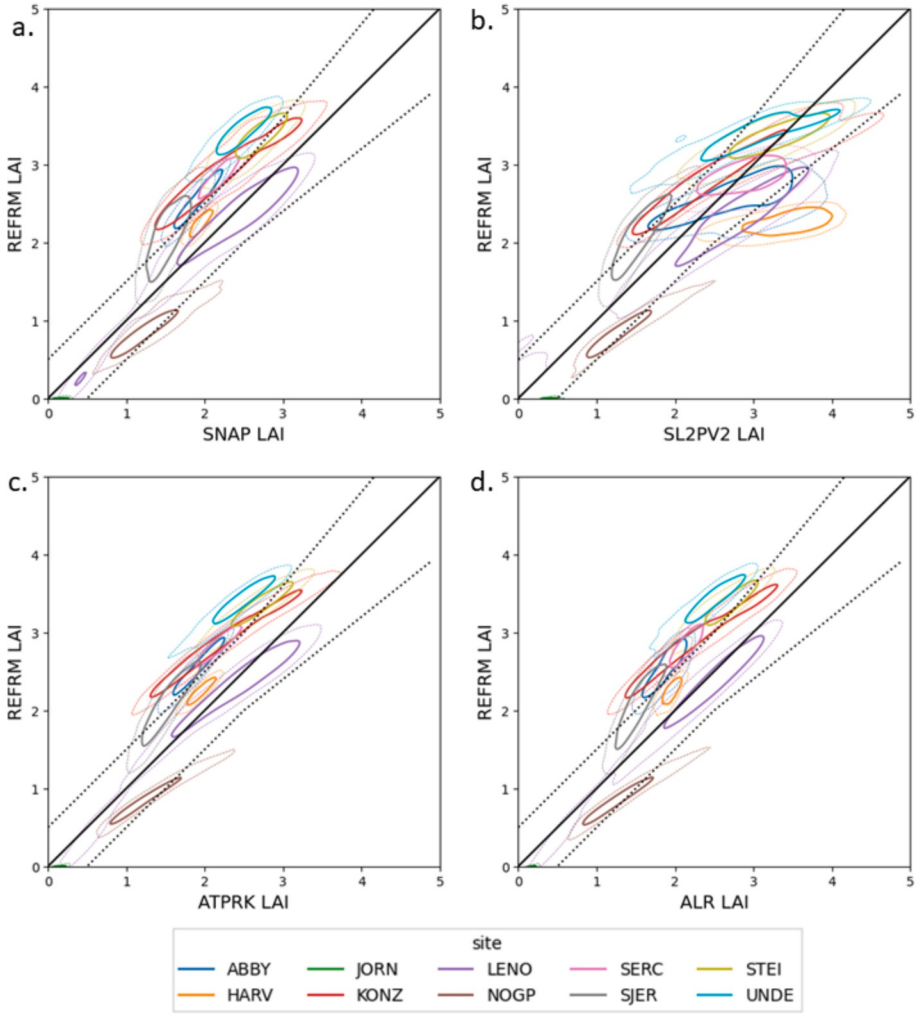


**Fig. 3.** Kernel density plots of estimated 10 m LAI from 20 m resolution AL2 imagery versus REFRM 10 m LAI for each site. Solid (dashed) contours correspond to 50 percentile (10 percentile) cumulative probability density. Dashed line corresponds to GCOS LAI uncertainty requirement, solid line corresponds to 1:1 line.

valid retrievals from either the REFRM or REFV1 10 m resolution reference LAI maps and estimates from each algorithm (Table 4). Comparisons to REFV1 maps assumed SL2PV1 is itself unbiased. These comparisons are relevant if a local bias correction, that accounts for canopy clumping, can be applied to the derived 10 m LAI maps. Comparisons to REFRM provide a traceable validation of derived 10 m LAI maps, without further bias correction, to fiducial reference measurements. Only pixels where all algorithms provided a valid retrieval were used to facilitate comparison of performance across algorithms. Kernel density plots of comparisons were produced for each site to visualize both the typical (50 percentile) and extreme (10 percentile) of the joint distribution of estimated and reference LAI in a manner independent of sample size. Site A, P, and U were computed from valid comparisons to test our hypothesis regarding the per-pixel estimation error while site average Pearson correlation coefficient (R) and structural similarity index measure (SSIM) (Wang et al., 2004), implemented in scikit-image (Van der Walt et al., 2014), were used to test our hypothesis regarding the fidelity of the spatial pattern of each estimate. R and SSIM were also

**Table 6**
Site uncertainty, accuracy, and precision, in units of LAI using REFRM as reference maps. Green indicates best methods within rounding error of 0.02. Forested sites indicated in bold.

| Site | U | | | | | A | | | | | P | | | | |
|---|---|---|---|---|---|---|---|---|---|---|---|---|---|---|---|
| | SNAP | ATPRK | ALR | SL2P V2 | BI-CUBIC | SNAP | ATPRK | ALR | SL2P V2 | BI-CUBIC | SNAP | AT-PRK | ALR | SL2P V2 | BI-CUBIC |
| *mean* | 0.55 | 0.54 | 0.55 | 0.57 | 0.55 | -0.36 | -0.36 | -0.36 | 0.15 | -0.36 | 0.19 | 0.15 | 0.16 | 0.35 | 0.19 |
| *range* | 0.77 | 0.78 | 0.77 | 0.79 | 0.77 | 1.40 | 1.41 | 1.43 | 1.63 | 1.40 | 0.24 | 0.18 | 0.19 | 0.43 | 0.25 |
| **ABBY** | 0.64 | 0.63 | 0.65 | 0.56 | 0.64 | -0.61 | -0.62 | -0.62 | 0.28 | -0.61 | 0.19 | 0.13 | 0.19 | 0.49 | 0.20 |
| **HARV** | 0.30 | 0.30 | 0.30 | 1.18 | 0.30 | -0.29 | -0.29 | -0.28 | 1.11 | -0.29 | 0.09 | 0.07 | 0.11 | 0.42 | 0.10 |
| JORN | 0.19 | 0.18 | 0.20 | 0.42 | 0.19 | 0.17 | 0.17 | 0.19 | 0.42 | 0.17 | 0.07 | 0.06 | 0.05 | 0.07 | 0.09 |
| KONZ | 0.68 | 0.66 | 0.66 | 0.50 | 0.68 | -0.63 | -0.62 | -0.63 | -0.19 | -0.63 | 0.26 | 0.24 | 0.21 | 0.46 | 0.25 |
| LENO | 0.26 | 0.22 | 0.20 | 0.52 | 0.26 | 0.08 | 0.09 | 0.10 | 0.37 | 0.08 | 0.25 | 0.20 | 0.16 | 0.36 | 0.25 |
| NOGP | 0.50 | 0.51 | 0.53 | 0.58 | 0.50 | 0.46 | 0.46 | 0.48 | 0.53 | 0.46 | 0.21 | 0.23 | 0.21 | 0.25 | 0.19 |
| **SERC** | 0.66 | 0.66 | 0.67 | 0.41 | 0.66 | -0.65 | -0.65 | -0.66 | 0.09 | -0.65 | 0.12 | 0.09 | 0.13 | 0.40 | 0.12 |
| **SJER** | 0.62 | 0.58 | 0.57 | 0.58 | 0.63 | -0.54 | -0.54 | -0.52 | -0.53 | -0.54 | 0.31 | 0.21 | 0.24 | 0.24 | 0.32 |
| **STEI** | 0.71 | 0.68 | 0.72 | 0.39 | 0.72 | -0.67 | -0.66 | -0.70 | -0.13 | -0.67 | 0.23 | 0.15 | 0.16 | 0.37 | 0.27 |
| **UNDE** | 0.96 | 0.96 | 0.96 | 0.60 | 0.96 | -0.94 | -0.95 | -0.95 | -0.40 | -0.94 | 0.16 | 0.13 | 0.15 | 0.45 | 0.17 |

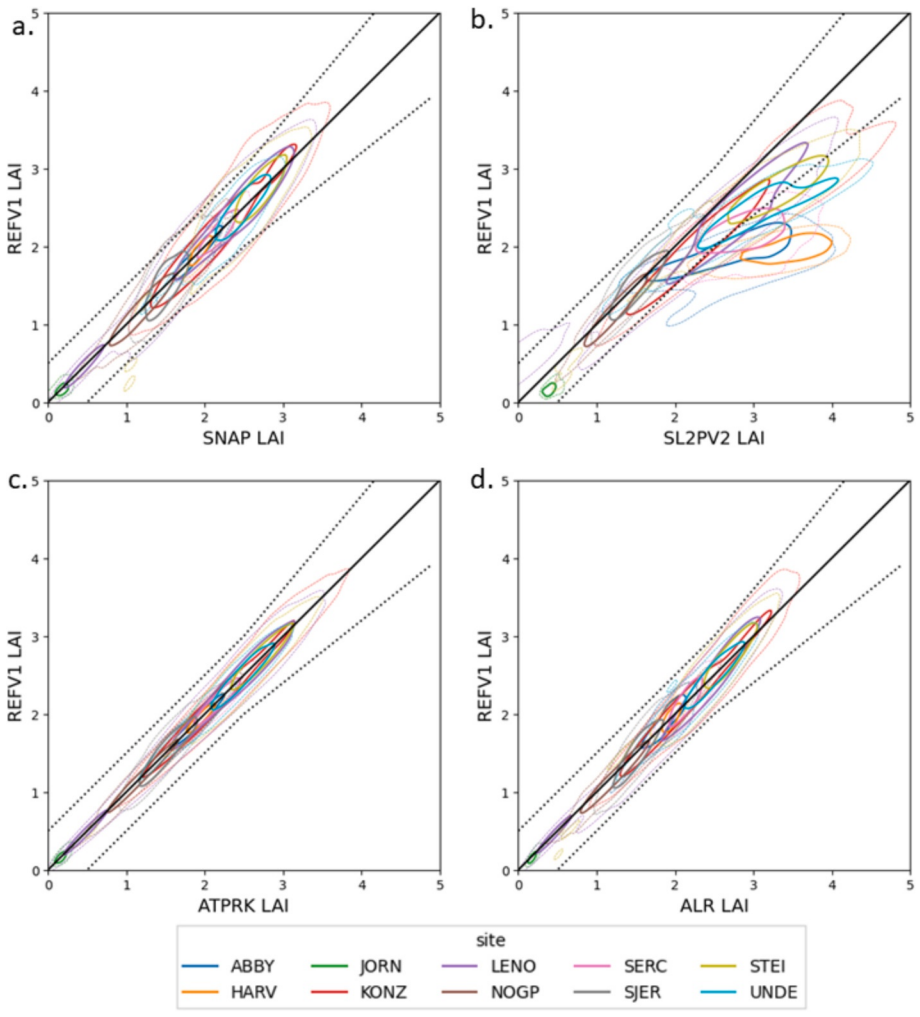


**Fig. 4.** Kernel density plots of estimated 10 m LAI from 20 m resolution AL2 imagery versus REFV1 10 m LAI for each site. Solid (dashed) contours correspond to 50 percentile (10 percentile) cumulative probability density. Dashed line corresponds to GCOS LAI uncertainty requirement, solid line corresponds to 1:1 line.

**Table 7**
Site uncertainty, accuracy, and precision, in units of LAI using REFV1 as reference maps. Green indicates best methods within rounding error of 0.02. Forested sites indicated in bold.

| Site | U | | | | | A | | | | | P | | | | |
|---|---|---|---|---|---|---|---|---|---|---|---|---|---|---|---|
| | SNAP | ATPRK | ALR | SL2P V2 | BI-CUBIC | SNAP | ATPRK | ALR | SL2P V2 | BI-CUBIC | SNAP | AT-PRK | ALR | SL2P V2 | BI-CUBIC |
| *mean* | 0.19 | 0.11 | 0.15 | 0.62 | 0.20 | 0.00 | 0.00 | 0.00 | 0.51 | 0.00 | 0.20 | 0.11 | 0.15 | 0.31 | 0.20 |
| *range* | 0.23 | 0.12 | 0.16 | 1.32 | 0.24 | 0.03 | 0.01 | 0.06 | 1.40 | 0.03 | 0.23 | 0.12 | 0.17 | 0.42 | 0.24 |
| **ABBY** | 0.12 | 0.08 | 0.14 | 1.02 | 0.13 | 0.01 | 0.00 | 0.00 | 0.89 | 0.01 | 0.12 | 0.08 | 0.14 | 0.50 | 0.13 |
| **HARV** | 0.10 | 0.07 | 0.11 | 1.46 | 0.10 | 0.01 | 0.00 | 0.01 | 1.40 | 0.01 | 0.10 | 0.07 | 0.11 | 0.41 | 0.10 |
| JORN | 0.08 | 0.05 | 0.05 | 0.25 | 0.08 | 0.00 | 0.00 | 0.01 | 0.24 | 0.00 | 0.08 | 0.05 | 0.04 | 0.07 | 0.08 |
| KONZ | 0.31 | 0.16 | 0.21 | 0.54 | 0.32 | -0.02 | 0.00 | -0.01 | 0.42 | -0.02 | 0.31 | 0.16 | 0.21 | 0.33 | 0.32 |
| LENO | 0.28 | 0.17 | 0.20 | 0.43 | 0.28 | -0.01 | 0.00 | 0.02 | 0.28 | -0.01 | 0.28 | 0.17 | 0.20 | 0.34 | 0.29 |
| NOGP | 0.20 | 0.09 | 0.12 | 0.14 | 0.20 | -0.01 | 0.00 | 0.02 | 0.06 | -0.01 | 0.20 | 0.09 | 0.12 | 0.13 | 0.21 |
| **SERC** | 0.13 | 0.09 | 0.14 | 0.85 | 0.13 | 0.01 | 0.00 | 0.00 | 0.75 | 0.01 | 0.13 | 0.09 | 0.14 | 0.40 | 0.13 |
| **SJER** | 0.23 | 0.14 | 0.17 | 0.17 | 0.24 | -0.01 | -0.01 | 0.01 | 0.01 | -0.01 | 0.23 | 0.14 | 0.17 | 0.17 | 0.24 |
| **STEI** | 0.19 | 0.11 | 0.15 | 0.62 | 0.20 | 0.00 | 0.00 | 0.00 | 0.51 | 0.00 | 0.20 | 0.11 | 0.15 | 0.31 | 0.20 |
| **UNDE** | 0.23 | 0.12 | 0.16 | 1.32 | 0.24 | 0.03 | 0.01 | 0.06 | 1.40 | 0.03 | 0.23 | 0.12 | 0.17 | 0.42 | 0.24 |

quantified as a function of the local coefficient of variation (CV) of REFRM within moving 110 m × 110 m windows across all sites. The sensitivity of site A and U to potential underestimation of RM LAI was evaluated by quantifying these metrics with REFRM maps scaled by % 105 and %110.

## 3. Results

### 3.1. Transfer function calibration

At each site, between 168 and 505 LAI samples were used for SL2PV1 LAI versus in-situ LAIe regressions and between 211 and 362 samples were used for in-situ LAIe versus in-situ LAI regressions (Table 5). The 67.5% PIs of both regressions covered the majority of measurements and were almost constant width with respect to the regressor (Appendix A). As such, the regression PIs were summarized using their mean 67.5% PI half width. The PI half widths for SL2PV1 LAI versus in-situ LAIe regressions ranged from 0.39 LAIe to 0.53 LAIe, except for the very low LAI JORN site where it was only 0.09 LAIe (Table 5). The PI for in-situ LAIe versus in-situ LAI ranged from 0.33 LAI to 0.45 LAI for forested sites and 0.01 LAI to 0.08 LAI otherwise. The estimated PI of the combined TF, corresponding to the uncertainty of REFRM LAI estimates, ranged from 0.30 LAI to 0.69 LAI with the exception of JORN where it was only 0.09 LAI. The relatively small PIs indicate that per-pixel differences of <0.68 can be detected with confidence 67.5% of the time. However, the impact of PI uncertainty on regional comparison statistics is likely negligible given that population statistics are based on all valid samples within a 1.5 km by 1.5 km window, and even the local SSIM statistic used a 121 sample widow.

The U, A and R2 for SL2PV1 applied at 10 m resolution were also quantified since SNAP, ALR and ATPRK rely on SL2PV1 and will propagate SL2PV1 biases. SL2PV1 bias ranged from −1.34 LAI to 0.2 LAI with underestimation at all sites except the JORN dry shrubland and NOGP grassland sites. Additionally, except for NOGP, over two thirds of uncertainty was due to accuracy error.

### 3.2. Validation

#### 3.2.1. Per-pixel metrics

When using AL2 inputs, site specific joint sample distributions of predicted versus REFRM LAI, were similar for SNAP, ATPRK and ALR (Fig. 3). Joint distributions for BICUBIC are given in Appendix F (Fig. F1) for brevity as they were very similar to SNAP. The majority of estimates for SNAP, ATPRK and ALR were within ±20% of the 1:1 line for grasslands and shrub sites but biased by ~20% above the 1:1 line for forests. In contrast, the joint distributions of SL2PV2 vs REFRM LAI showed the least symmetry parallel to the 1:1 line, with substantial skew over forested sites and bias of between −10% and − 20% over grassland and crop sites. However, in comparison to other algorithms, the SL2PV2 vs REFRM LAI distributions showed lower bias over forests for LAI > 2, except for HARV where SL2PV2 underestimated LAI by 1.18 LAI on average (Table 6). Joint distributions of predicted versus REFRM LAI based on L2 inputs (Appendix D) were qualitatively similar to those of the RM versus AL2 comparisons in terms of bias. However, the RM versus L2 comparisons indicated greater scatter than the RM versus AL2 comparisons. This was expected given mis-registration and radiometric normalization error between the corresponding AHS reference maps and L2A products.

Joint distributions of predicted versus REFV1 LAI showed far less dispersion and bias in comparison to their predicted versus REFRM LAI counterparts (compare Fig. 3 and Fig. 4). Irrespective of land cover, ATPRK and ALR joint distributions were concentrated along the 1:1 line with the majority of their retrievals corresponding to an agreement with REFV1 LAI better than 10%. SNAP versus REFV1 LAI joint distributions were also generally along the 1:1 line, but the dispersion was almost twice that observed for ATPRK and ALR counterparts. SL2PV2 versus REFV1 LAI joint distributions showed the largest dispersion and least symmetry amongst algorithms, with a large negative bias at the HARV forested site and positive bias for the LENO crop/grassland site.

When compared to REFRM maps, the mean U across all sites was ~0.55 LAI for BICUBIC, SNAP, ATPRK and ALR, with SL2PV2 slightly worse at 0.57 LAI (Table 6**Error! Reference source not found.**). Additionally, BICUBIC and SNAP metrics were virtually identical. That said, for a given algorithm, the between site range in U was substantial at ≥0.77 LAI. For example, SL2PV2 had the lowest U at all forested sites except HARV, ranging from 0.44 LAI to 0.61 LAI, even though it had the largest mean U. Accuracy closely followed the pattern observed for U, with SL2PV2 having less than half the bias of the other algorithms at four of the forested sites; resulting in a mean A of 0.15 LAI for SL2PV2 versus ~ − 0.36 LAI for other approaches. ATPRK and ALR resulted in

**Table 8**
Site R, SSIM. Green indicates best methods within rounding error of 0.02. Forested sites indicated in bold. #samples correspond to count of valid 10 m pixels used for comparisons.

| Site | R | | | | | SSIM | | | | | #samples |
|---|---|---|---|---|---|---|---|---|---|---|---|
| | SNAP | ATPRK | ALR | SL2PV2 | BICUBIC | SNAP | ATPRK | ALR | SL2PV2 | BICUBIC | |
| *mean* | 0.72 | 0.86 | 0.85 | 0.77 | 0.72 | 0.77 | 0.84 | 0.83 | 0.70 | 0.77 | 6091 |
| *range* | 0.67 | 0.44 | 0.27 | 0.41 | 0.73 | 0.61 | 0.64 | 0.65 | 0.78 | 0.60 | 3841 |
| **ABBY** | 0.82 | 0.90 | 0.83 | 0.64 | 0.83 | 0.84 | 0.90 | 0.87 | 0.65 | 0.83 | 4586 |
| **HARV** | 0.71 | 0.85 | 0.69 | 0.54 | 0.71 | 0.92 | 0.95 | 0.92 | 0.61 | 0.91 | 6699 |
| JORN | 0.19 | 0.52 | 0.69 | 0.59 | 0.15 | 0.31 | 0.31 | 0.28 | 0.09 | 0.28 | 7504 |
| KONZ | 0.81 | 0.94 | 0.93 | 0.92 | 0.83 | 0.82 | 0.90 | 0.91 | 0.88 | 0.82 | 6546 |
| LENO | 0.82 | 0.91 | 0.92 | 0.86 | 0.83 | 0.84 | 0.91 | 0.93 | 0.82 | 0.83 | 3663 |
| NOGP | 0.86 | 0.96 | 0.95 | 0.95 | 0.88 | 0.86 | 0.87 | 0.87 | 0.85 | 0.87 | 6840 |
| **SERC** | 0.76 | 0.87 | 0.76 | 0.63 | 0.77 | 0.87 | 0.91 | 0.88 | 0.64 | 0.87 | 5841 |
| **SJER** | 0.72 | 0.89 | 0.89 | 0.86 | 0.73 | 0.63 | 0.82 | 0.79 | 0.80 | 0.61 | 6242 |
| **STEI** | 0.79 | 0.91 | 0.90 | 0.87 | 0.72 | 0.85 | 0.91 | 0.91 | 0.84 | 0.81 | 6725 |
| **UNDE** | 0.77 | 0.89 | 0.89 | 0.86 | 0.78 | 0.82 | 0.88 | 0.88 | 0.80 | 0.81 | 6266 |

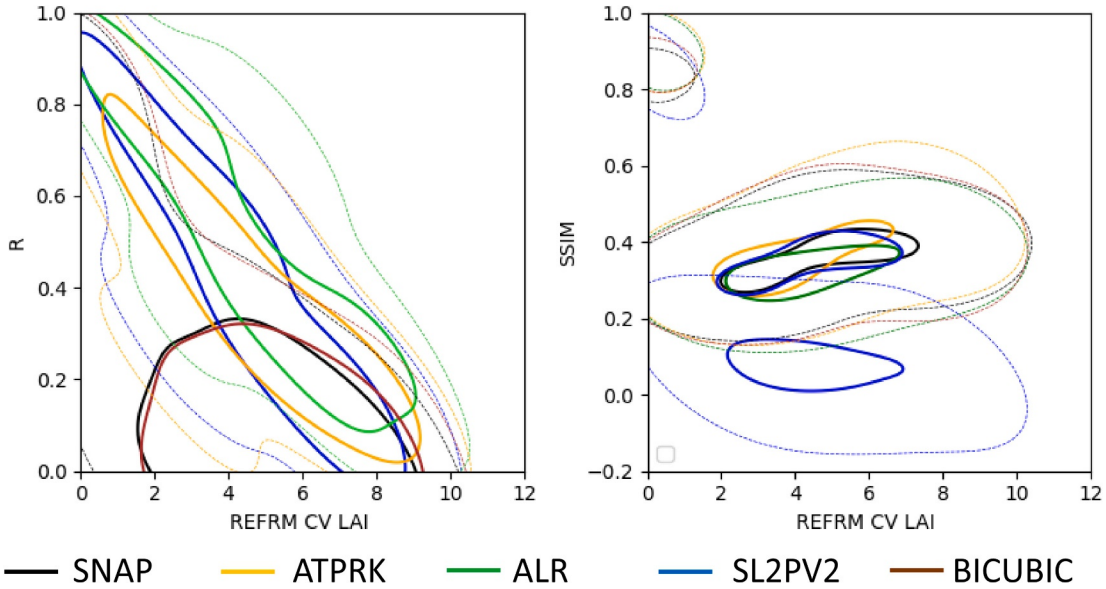


**Fig. 5.** Kernel density plots of conditional distribution of the(a.) Pearson correlation coefficient I and (b.) Structural Similarity Image Metric (SSIM) (right panel) versus reference LAI coefficient of variation (REFRM CV LAI) for 110 m × 110 m moving windows using input AL2 imagery. Solid (dashed) contours correspond to 50 percentile (10 percentile) cumulative probability density.

the lowest mean precision error of ~0.15 LAI with ATPRK P being slightly lower on a site-by-site basis. SNAP and BICUBIC P was only slightly (~0.03 LAI) larger than ALR on average but could be up to 0.14 LAI higher on a site basis. SL2PV2 had a much greater P error that the other algorithms, averaging 0.47 LAI and only once dropping below 0.25 LAI. In summary, when compared to REFRM maps, SL2PV2 had the lowest mean accuracy error but mean uncertainty was approximately equal across algorithms. Furthermore, ALR and ATPRK had the lowest precision error at most sites.

When compared to REFV1 maps, the mean U across all sites was <0.20 LAI for SNAP, AAPRK and ALR, with ATPRK always resulting in the lowest U. SL2PV2 resulted in the highest average U of 0.62 LAI (Table 7). For all algorithms except SL2PV2, the range in U was much smaller than observed for comparisons to REFRM maps. Also, all algorithms except SL2PV2 had an absolute accuracy error <0.05. This was expected given that both their estimates and the REFV1 maps are based on SL2PV1. In contrast SL2PV2 overestimated REFV1 LAI by 0.51 LAI on average, and up to 1.4 LAI (at the HARV site). Precision error was lowest for ATPRK at all sites with a mean error of 0.11 LAI with ALR slightly worse at 0.15 LAI and SNAP and BICUBIC at 0.20 LAI. Precision error for SL2PV2 was greater than the other approaches at all sites, with a mean P of 0.31 LAI. In summary, when compared to REFV1 maps, ATPRK was always the best algorithm in terms of A,P and U although ALR was close at most sites. Furthermore, SL2PV2 was almost always the worst in terms of A, P, and U; although one should keep in mind that the REFV1 maps are themselves biased estimates of in-situ LAI.

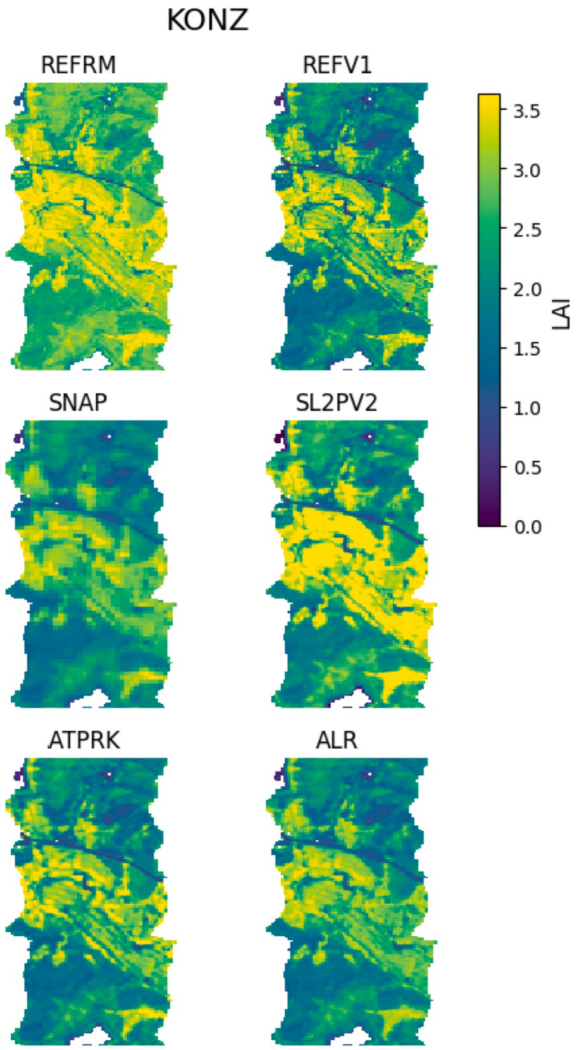


**Fig. 6.** 10 m resolution LAI maps based on input 10 m synthetic imagery for S2 bands (REFRM and REFV1) and input synthetic S2 imagery (SNAP, SL2PV2, ATPRK, ALR) for KONZ site. White areas correspond to invalid retrievals.

### 3.2.2. *Spatial agreement metrics*

R and SSIM were consistent with the precision error results, with ATPRK and ALR resulting in the best mean and site specific statistics, and SNAP and BICUBIC the worst statistics, when compared to REFRM maps (Table 8) or REFV1 maps (Appendix D). There were only two sites, NOGP and SERC, where SL2PV2 showed similar R or SSIM statistics to ATPRK and ALR, and no sites where SNAP matched ATPRK for R and SSIM. In fact, BICUBIC, SNAP and SL2PV2 has similar mean R and SSIM, although their performance was not consistent across sites. In summary, as observed with precision error, ATPRK and ALR shared the best results, and SNAP and SL2PV2 the worst results, for both site specific and mean R and SSIM.

The conditional distributions of R and SSIM with respect to REFRM CV LAI were used to quantify how well each algorithm represented local LAI patterns as a function of pattern complexity (Fig. 5). Except for SNAP AND BICUBIC, the typical R was inversely proportional to CV LAI, ranging from $R > 0.8$ for CV LAI $< 1$ to $R < 0.2$ for CV LAI $> 5$. SNAP and BICUBIC had very similar distributions, with the typical R was always $<0.36$ and was essentially unrelated to CV LAI. Similar relationships were observed between R and CV LAI for less likely samples although the spread of these contours was about twice that observed for typical cases in Fig. 5. In contrast to R, for typical cases, SSIM did not show a clear relationship with CV LAI, ranging from $0.05 <$ SSIM$<0.15$ for SL2PV2 and $0.25 <$ SSIM$<0.45$ for the other algorithms. As with R versus CV LAI, the contours for SSIM vs CV LAI were about twice as broad for less likely cases as for the typical cases. However, there was also a high SSIM mode for less likely cases, corresponding to regions with low local variation, with SSIM$>0.7$ and CV LAI $< 0.2$, that was generally indistinguishable across algorithms. In summary, ALR and ATPRK ranks highest for both R and SSIM conditional on CV LAI while SNAP ranks lowest for R conditional on CV LAI and SL2PV2 ranks lowest for SSIM conditional on CV LAI.

### 3.2.3. *Qualitative Intercomparisons*

Qualitative intercomparisons based on visual assessment of images are widely used to evaluate downscaling algorithms. Comparisons were performed at all sites to sample different land cover and LAI pattern complexity (Appendix E and F). For brevity, R and SSIM results for all methods except BICUBIC are shown for two sites that inform the previous precision are presented here. BICUBIC results are provided in Appendix F as they are similar to SNAP in appearance.

The KONZ site corresponds to a mosaic of forest and grassland land cover with relatively uniform LAI patches at 20 m resolution but with cast shadows and mixed pixels at edges between canopies of different heights (Fig. 6). REFRM and REFV1 reference maps are qualitatively similar, with the former essentially a positively biased version of the

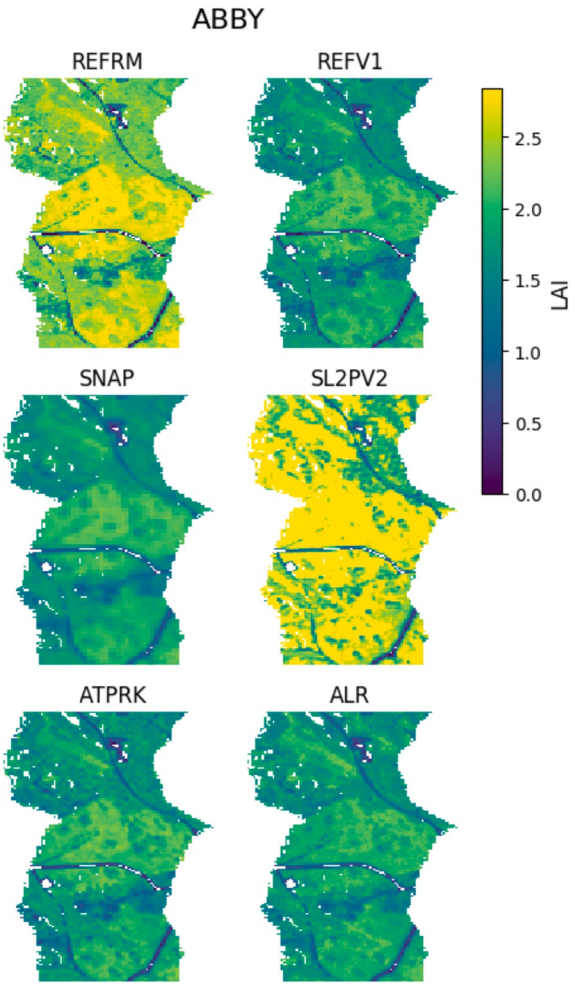


**Fig. 7.** 10 m resolution LAI maps based on input 10 m synthetic imagery for S2 bands (REFRM and REFV1) and input synthetic S2 imagery (SNAP, SL2PV2, ATPRK, ALR) for SJER site. White areas correspond to invalid retrievals.

latter as expected when converting LAIe to LAI. Single pixel wide roads and linear clearings, as well as within forest texture, are clearly visible in both REFRM and REFV1 maps. Both ATPRK and ALR represent REFRM spatial patterns well, with ATPRK better at capturing the high LAI region of forests. SNAP appears as if a $2 \times 2$ blurring filter was applied to ALR. SL2PV2 exaggerates both high and low LAI values, almost saturating within some forested areas (central region in Fig. 6). However, SL2PV2 also tends to represent the variability within moderate LAI forests in the north of the site better than the other approaches.

The ABBY site corresponds to a region with a range of forest types and densities intersected by single pixel roads (Fig. 7). Mixed pixels occur along roads, but otherwise LAI variation occurs within large patches. Only SL2PV2 captures the magnitude of REFRM LAI well over forests, but at the cost of missing detail of within-patch LAI patterns. Results are quite different when comparing algorithms to REFV1 LAI. Here ALR is close in magnitude and pattern to REFV1 LAI, with ATPRK only slightly blurrier. SNAP results in the same visually obvious spatial blurring observed at KONZ. SL2PV2 appears to quantize the REFV1 LAI pattern into a few, exaggerated, levels but retains spatial detail at edges.

## 4. Discussion

### 4.1. Study scope

To our knowledge, this is the first study to validate high ($\leq$10 m) resolution LAI maps following community good practice guidelines with traceability to in-situ fiducial reference measurements. Previous studies have resorted to validating high resolution maps by scaling them to match lower resolution reference maps (Houborg and McCabe, 2018; Kganyago et al., 2020) or by only considering spatially homogeneous reference sites such as croplands (Kross et al., 2015; Kimm et al., 2020). Other studies have used gap fraction based reference measurements, such as LAIe, with spatial footprints >10 m resolution and without correction for non-photosynthetic matter (Colombo, 2003; Soudani et al., 2006). These approaches test necessary, but not sufficient, conditions to support the hypothesis that the high-resolution mapping algorithms are either accurate or precise. Indeed, none of these approaches validate retrievals of complex spatial patterns and retrievals across edges between different canopies that are amongst the primary motivations for producing 10 m LAI maps.

Our scope was limited to validating one candidate algorithm from each of five differing approaches to producing 10 m resolution S2 LAI maps. In fact, two other downscaling algorithms were initially involved, but dropped either due to visible artifacts (DSEN2, Lanaras et al., 2018) or dependencies on closed libraries (SEN2RES, Brodu, 2017) that could not be easily applied to the synthetic S2 imagery. We will be publishing our reference maps as an open dataset (Fernandes et al., in review) to allow the community to test novel approaches in a controlled manner.

### 4.2. Reference LAI maps

The validation protocol was the most challenging part of this study.

Ideally, one would use ≤10 m resolution reference maps produced using in-situ spatial surveys of RM matched to high resolution imagery with an associated TF relating them to in-situ RM. This is not currently possible as non-destructive fiducial RM of LAI are only widely available using gap fraction analyses methods corresponding to a spatial support exceeding the canopy height (Weiss et al., 2004; Fernandes et al., 2023). Mono-directional contact methods (Law et al., 2021, Gebbers et al., 2011), three-dimensional terrestrial laser scanning systems (Hosoi and Omasa, 2006; Béland et al., 2011; Dube et al., 2019) and structure from motion processing of high resolution imagery (dos Santos et al., 2020) have been shown to estimate LAI for small (≤10 m) horizontal footprints given assumptions regarding leaf angle distribution. These methods may allow for high-resolution LAI maps in the future but their current cost, availability and, more importantly, maturity as fiducial RM currently inhibit their use for validating 10 m resolution LAI maps over multiple sites.

Initially, our experiment tested each algorithm using S2 L2B products as input (L2). Indeed, this was one reason we did not exploit all the available NEON AHS data. This approach was flawed from the point of view of algorithm validation because differences in atmospheric correction and geolocation between the reference maps and the input to downscaling algorithms resulted in experimental errors that masked differences between the tested algorithms. While we reduced these errors by radiometric cross-calibration, the precision of comparisons based on L2 products was lower than that using synthetic S2 imagery (AL2) products derived from the same imagery used for the reference map (compare Fig. 3 and Appendix D Fig. D1). We suspect that future validation experiments may need to rely on synthetic S2 imagery unless great care is performed to match footprints of individual reference measurements to footprints of high resolution products and to characterize the uncertainty due to input reflectance measurement error. That said, we still included comparisons based on actual S2 imagery (Appendix B) as they verified that our results based on synthetic imagery were consistent with applying high resolution LAI mapping algorithms to S2 imagery. Indeed, it is the observed consistency between results based on S2 and AHS input imagery that leads us to recommend future studies use the synthetic image approach to exploit all available NEON AHS imagery.

Validation using SL2PV1 reference imagery resulted in ALR and ATPRK being both almost unbiased and relatively precise, considering GCOS requirements, at all sites, with BICUBIC and SNAP slightly worse. While BICUBIC and SNAP were close to ALR and ATPRK in terms of A and U, qualitative visual assessment and quantitative spatial metrics indicated the latter two approaches resulted in much better spatial agreement with SL2PV1 estimated LAI. In contrast, SL2PV2 had lower precision at most sites and positive bias over forested sites when compared to SL2PV1 imagery. SL2PV2 overestimation of forests LAI persisted when using input bands averaged to 60 m (not shown) suggesting that it was not due to its use of a radiative transfer model that assumes of zero lateral fluxes between pixels, i.e. that shadows or scattered light from adjacent pixels can be neglected (Verhoef, 1984). Instead, we hypothesize that the overestimate was due to biases in input red reflectance over low reflectance targets such as forests, although testing this hypothesis is beyond the scope of our study. These would have been our conclusions if, as in many other studies using either effective LAI as reference or simply relying on algorithm intercomparisons, we did not insist on 10 m resolution reference maps traceable to in-situ LAI (REFRM). However, we would have been wrong since our results were completely different when using REFRM maps as reference.

Considerable effort was required to produce the REFRM maps. We could not simply apply a TF calibrated using matching REFV1 LAI retrievals and in-situ RM since the latter were not available at 10 m resolution. The first stage, converting SL2PV1 LAI to LAIe, was employed specifically because SL2PV1 is known a priori to assume a homogenous canopy and subsequently is approximately linearly related to LAIe at the same scale (Brown et al., 2020). Using a linear transfer function ensured the calibration based on the spatial support of the in-situ DHP footprints was unbiased when applied at 10 m resolution. Robust linear regression also reduced the impact of random errors in conversion factors between PAIe and LAIe applied based on in-situ databases. Ideally, these factors would be calibrated locally using leaf-off samples for deciduous land cover, or methods capable of leaf-wood separation such as near-infrared DHP or dual-wavelength terrestrial laser scanning (Brown et al., 2024; Danson et al., 2018). Such data were not available over the NEON sites. As such, we resorted to typical values of woody to total area ratios for our forest sites with an associated uncertainty of ~10% (Brown et al., 2021a). Some of this uncertainty will persist in biases in the final transfer function but, except for SJER, differences between SL2PV2 and the other algorithms are far >10% in terms of accuracy (Table 5).

The second stage, which corrects for within pixel canopy clumping and non-photosynthetic vegetation, relied solely on paired in-situ RM of LAI and LAIe. Fortuitously, the error in assuming a constant ratio of LAIe to LAI was reasonable (PI typically <0.5 LAI and R2 > 0.9), perhaps because the NEON sites are in landscapes with low within site variability in land cover and vegetation patterns. As a result, the per-pixel PIs of the final REFRM LAI maps were modest (<0.7 LAI). Moreover, the clumping calibration assumes the clumping index for in-situ sites also applies at 10 m resolution. This assumption is difficult to verify since estimation of clumping requires second order spatial statistics sampled over extents greater than the largest canopy gaps (Lang and Xiang, 1986). That said, validation population statistics were derived from between 3663 and 7504 samples, so our major concern was not the PI but bias of the REFRM maps due to measurement errors, spatial or temporal mismatch, and error in the regression model. Thiel-Sen regression was used to reduce the likelihood the TF was unbiased. In fact, there is no unbiased linear regression estimator for random measurement errors but at least Thiel-Sen results in a statistically consistent estimator that converges to the unbiased estimator under mild assumptions and with <28% outliers (Fernandes and Leblanc, 2005). The use of other linear regression approaches for calibrating local TFs, within other studies, is baffling given that they are not even statistically consistent slope estimators. The Thiel-Sen PI was at least twice as large as the regression U (root mean square error). This suggests that TF error propagation based on population U may be optimistic as recommended by current good practice (Fernandes et al., 2014). The sensitivity of A and U to correcting for hypothetical 5% and 10% underestimates due to clumping bias resulted in proportional changes in A and somewhat smaller relative changes in U due to the presence of precision error but the relative ranking of methods did not change overall and for plots. (Appendix G).

### 4.3. Direct validation performance

Repeating our experiment using REFRM reference maps resulted in drastic differences in per-pixel metrics compared to the same metrics derived using REFV1 maps. Now, SL2PV2 was close to being unbiased at most sites, while the other algorithms underestimated LAI at forest sites. Some of the improvement in SL2PV2 bias may be due to its ability to account for landscape level clumping between 10 m pixels. However, the downscaled images indicate patches of high LAI over forests with poor spatial agreement to REFRM imagery (e.g. the upper half of the ABBY image in Fig. 7) and ALR did not result in unbiased forest LAI retrievals even though it also only uses 10 m bands. We hypothesize that the SL2PV2 bias reduction is possibly a fortuitous cancellation of LAI underestimation due to SL2PV2 using a homogenous radiative transfer model during calibration and LAI overestimation due to errors in input reflectance. The ATPRK, BICUBIC and SNAP bias could possibly be due to unresolved spatial smoothing of, respectively, SL2PV1 inputs or SL2PV1 outputs. But this does not explain why ALR, that only uses 10 m resolution input bands, was also biased or why ATPRK showed good spatial agreement with REFRM. We hypothesize that ALR encodes bias when using 20 m pixels during calibration of its local regression

estimator. The induced bias is simply because local LAI versus vegetation index regressions are only scale independent if both the vegetation index manner and the actual LAI versus vegetation index relationship is scale independent (Garrigues et al., 2006). Indeed, Table 5 indicates negative bias ranging from −0.4 LAI to −1.34 LAI for all but two sites. This result underlines the fact that downscaling algorithms tested do not address bias in the underlying SL2PV1 algorithm due to canopy scale clumping (Brown et al., 2021a). Land cover specific versions of SL2PV1 with reduced bias are available (Fernandes et al., 2024a) but would require 10 m land cover maps that would induce additional uncertainty in 10 m LAI maps produced by ATPRK, SNAP, BICUBIC or ALR.

Both R and SSIM spatial agreement metrics were reported in our study. The negative correlation of R with CV LAI reflects the fact that the spatial precision of downscaling algorithms decreases in areas with complex spatial patterns. In contrast SSIM was uncorrelated with CV LAI for most of the tested scenes, suggesting it may be a more appropriate statistic when comparing downscaling performance across different studies. ATPRK and ALR had the best precision and spatial agreement metrics while SL2PV2, SNAP and BICUBIC were worse in most circumstances. The inferior performance of BICUBIC and SNAP, especially for areas with high local CV LAI, was expected since they rely only on spatial proximity to enhance resolution. High spatial frequency measurement errors, such as band-to-band misregistration, is unlikely to explain the inferior performance of SL2PV2 as it would also apply to ALR, that uses the same 10 m input bands. Again, we hypothesize the poor SL2PV2 spatial metrics, especially SSIM, may be due to input measurement error resulting in saturation for forests that can have low visible reflectance (Butson and Fernandes, 2004). ALR is subject to the same input reflectance error as SL2PV2 as it also uses only 10 m resolution bands. This prompts the question as to why ALR did not also show the same saturation as SL2PV2. We hypothesize that the regularization incorporated in ALR reduces its sensitivity to measurement errors since ALR forces outlier retrievals into the space of valid retrievals. Indeed, ALR was originally used to revise SL2PV1 retrievals flagged as invalid due to input measurement error (Djamai and Fernandes, 2021).

Our study indicates that there is a bias-variance trade-off for algorithms mapping LAI at 10 m resolution using S2. SL2PV2 offers a bias generally under 0.5 LAI while ATPRK and ALR offer a precision of ~0.16 LAI, but all methods have similar total uncertainty of ~0.55 LAI. ATPRK or ALR may be suitable for 10 m resolution S2 maps if their bias could be reduced. Current bias correction approaches are land cover dependent; a luxury that may not be afforded at 10 m resolution in changing landscapes. Alternatively, combining SL2PV1 and either ALR or ATPRK may reduce the uncertainty of 10 m resolution S2 LA maps.

### 4.4. Limitations and recommendations

This study serves as a starting point for validating high spatial resolution LAI maps. Reported A and U for REFRM comparisons may be optimistic for BICUBIC, SNAP, ALR and ATPRK due to uncertainties associated with clumping correction. Clumping was a major issue when producing reference maps. Our method requires a TF to correct for clumping that depends on unbiased in-situ clumping estimates and representative sampling for each site. Fortuitously, the clumping transfer functions supported our assumption of constant site clumping. Even so, extending our approach to other sites will require reference measurements of clumping. High resolution LIDAR imaging and structure for motion surveys has both been used to produce LAI maps at ≤10 m resolution (Fang et al., 2019). However, both approaches currently require calibration to in-situ measurements (Lefsky et al., 2002; Kamoske et al., 2018; Mendes dos Santos et al., 2020; Sumnall et al., 2021; Awaya and Araki, 2023). This calibration would need to adopt our assumption clumping does not change between the DHP footprint and 10 m grids. More limiting for LIDAR surveys is the finding from Kamoske e et al. 2019 that the LIDAR PAIe estimates at SERC could not quantify understory LAI. Nevertheless, both LIDAR and structure from motion surveys could potentially provide better spatial delineation of relative LAI patterns than the 1 m resolution AHS imagery that suffers from potential shadowing between pixels.

Our study was limited in being able to validate only peak growing season conditions due to the timing of the AHS imagery. Future studies should consider multi-temporal validation but may need to enhance in-situ sampling since the assumption of a constant canopy clumping index may not hold. We hope the reader takes to heart our insistence to using reference maps traceable to in-situ fiducial reference measurements, rather than intercomparisons or off-line error propagation of downscaled reflectance product uncertainty. We would have arrived at vastly different conclusions if we took the easy way out and used only intercomparisons to reference maps derived using the SL2PV1 algorithm, rather than traceable reference maps. We also note that validation metrics varied between sites and between land cover. This variability underlines the importance of not drawing conclusions based on single site studies and the importance of using protocols that can be applied across space and time. We hope that both our methodology and the NEON datasets will enable further testing and refinement of algorithms for high-resolution LAI mapping.

## 5. Conclusions

Our study validated four differing approaches for producing 10 m resolution LAI maps using actual and simulated S2 imagery: simply interpolating 20 m resolution maps produced by applying the SL2PV1 algorithm (SNAP), using a global algorithm with input 10 m resolution bands (SL2PV2), using a local algorithm using only 10 m resolution bands (ALR), or spatial downscaling of input reflectance using bi-cubic interpolation (BICUBIC) or kriging followed by applying the 20 m resolution SL2PV1 algorithm. Results with simulated S2 inputs were used to assess algorithms as they did not suffer from measurement and geolocation error when comparing downscaled S2 LAI maps to reference maps.

When validated against reference 10 m LAI maps traceable to in-situ fiducial reference measurements of LAI at ten NEON sites, SL2PV2 resulted in the lowest overall bias (0.15 LAI) with <50% of the bias observed for other algorithms over most forested sites. However, ATPRK and ALR algorithms had the least precision error (~0.15 LAI) and ranked highest in terms of local correlation and Structural Similarity Index measure at all sites. Moreover ATPRK, and to some extent ALR, provided the best qualitative reproduction of the relative LAI pattern and the lowest residuals across all sites when compared to reference maps proportional to effective LAI. BICUBIC and SNAP approaches had similar bias to ATPRK and ALR but fared worse in terms of spatial metrics and resulted in visually blurred 10 m LAI maps. These results contradict our initial hypotheses that SL2PV2 would have the greatest bias on the basis that it does not use optimal input spectral sampling. This leads us to now hypothesize that the ATPRK and ALR forest LAI underestimation may be due to the use of a spatially homogeneous radiative transfer models for calibrating all algorithms. If true, then the low SL2PV2 bias observed here may actually be an artifact due to opposing model and input measurement errors.

Future studies are required to investigate strategies for correcting scale dependencies in LAI retrieval algorithms. For example, Fernandes et al. (2024) showed that modifying SL2PV1 with a spatially heterogeneous radiative transfer model resulted in a 61% reduction in bias over forests. This new algorithm may address the observed bias in the downscaled products that relied on SL2PV1. Finally, we encourage algorithm developers to make use of our methodology and datasets for validation and we encourage the development of new methods for high spatial resolution survey of in-situ LAI fiducial reference measurements.

## CRediT authorship contribution statement

**Richard Fernandes:** Writing – review & editing, Writing – original

draft, Visualization, Validation, Supervision, Software, Methodology, Formal analysis, Conceptualization. **Gang Hong:** Writing – review & editing, Visualization, Validation, Methodology, Investigation. **Luke A. Brown:** Writing – review & editing, Visualization. **Jadu Dash:** Validation. **Kate Harvey:** Software, Methodology. **Simha Kalimipalli:** Software, Validation. **Camryn MacDougall:** Software, Methodology. **Courtney Meier:** Writing – review & editing, Validation. **Harry Morris:** Writing – review & editing, Validation. **Hemit Shah:** Software, Methodology. **Abhay Sharma:** Software, Methodology. Lixin Sun: Software.

## Declaration of competing interest

The authors declare that they have no known competing financial interests or personal relationships that could have appeared to influence the work reported in this paper.

## Data availability

Data will be made available on request.

## Acknowledgements

SL2PV1 and SL2PV2 neural networks were produced using code adapted from original code provided by Dr. Marie Weiss and Dr. Fred Baret. We acknowledge the use of modified Sentinel-2 data and derived products. This study has been undertaken using data from GBOV "Ground Based Observation for Validation" (https://land.copernicus.eu/global/gbov) funded by European Commission Joint Research Centre FWC932059, part of the Global Component of the European Union's Copernicus Land Monitoring Service. GBOV products are developed and managed by ACRI-ST with the support from University College London, University of Leicester, University of Southampton, University of Valencia and Informus GmbH. We thank the National Ecological Observatory Network for the measurements collected in the field and used to generate GBOV products. We thank Dr. Marie Weiss and Dr. Fred Baret for providing the code used to calibrate SL2PV1 and SL2PV2. We thank four excellent reviewers and the editors of this paper. The contribution of L.A. Brown was carried out under the Living Planet Fellowship, a programme of and funded by the European Space Agency. The view expressed in this publication can in no way be taken to reflect the official opinion of the European Space Agency. The work was funded by Natural Resources Canada's Earth Observation for Cumulative Effects Project.

## Appendix A. Abbreviations

| Abbreviation | Description |
|---|---|
| A | Accuracy |
| A1m | image of 1 m S2 equivalent spectral bands |
| A1m | image of 10TFm S2 equivalent spectral bands |
| ABBY | Abby Road |
| AHS | Airborne Hyperspectral Imagery |
| AL2 | synthetic S2A image with nominal S2 band resolution |
| ALR | Active Learning Regularization |
| Arcsec | arc second |
| ATPRK | Area to Point Regression Kriging ( |
| B | Baseline |
| BICUBIC | Bi-Cubic Spline Interpolation of 20 m reflectance |
| DHPs | digital hemispherical photographs |
| ESU | Elementary sampling unit |
| G | Goal |
| GCOS | Global Climate Observing System |
| HARV | Harvard Forest |
| JORN | Jornada Experimental Range |
| KONZ | Konza Prairie Biological Station |
| L2 | Copernicus Sentinel-2 A and Sentinel-2B Level 2A Collection 1 surface reflectance products |
| LAI | Leaf Area Index |
| LAIe | effective LAI |
| LENO | Lenoir Landing |
| mrad | milliradian |
| NEON | National Ecological Observatory Network |
| NOGP | Northern Great Plains Research Laboratory |
| PAI | plant area index |
| PAIe | effective PAI |
| PI | 1 standard deviation prediction confidence interval |
| R | Precision |
| R2 | Coefficient of determination |
| REFRM | reference 10 m LAI map with traceability to in-situ RM |
| REFV1 | reference 10 m LAI map without traceability to in-situ RM |
| RM | Reference measurement |
| S2 | Sentinel 2 |
| SERC | Smithsonian Environmental Research Center |
| SJER | San Joaquin Experimental Range |
| SL2P | Simplified Level 2 Prototype Processor |
| SL2PV1 | Simplified Level 2 Prototype Processor Version 1 |
| SL2PV2 | Simplified Level 2 Prototype Processor Version 2 |
| SNAP | Sentinel Applications Platform |
| SSIM | Structural similarity index measure |
| STEI | Steigerwaldt-Chequamegon |
| T | Threshold |

(*continued on next page*)

(*continued*)

| Abbreviation | Description |
|---|---|
| TF | Transfer function |
| U | Uncertainty |
| UNDE | University of Notre Dame Environmental Research Center |
| ρ | Surface reflectance |

## Appendix B. Flowchart of methods for deriving downscaled products from L2 imagery

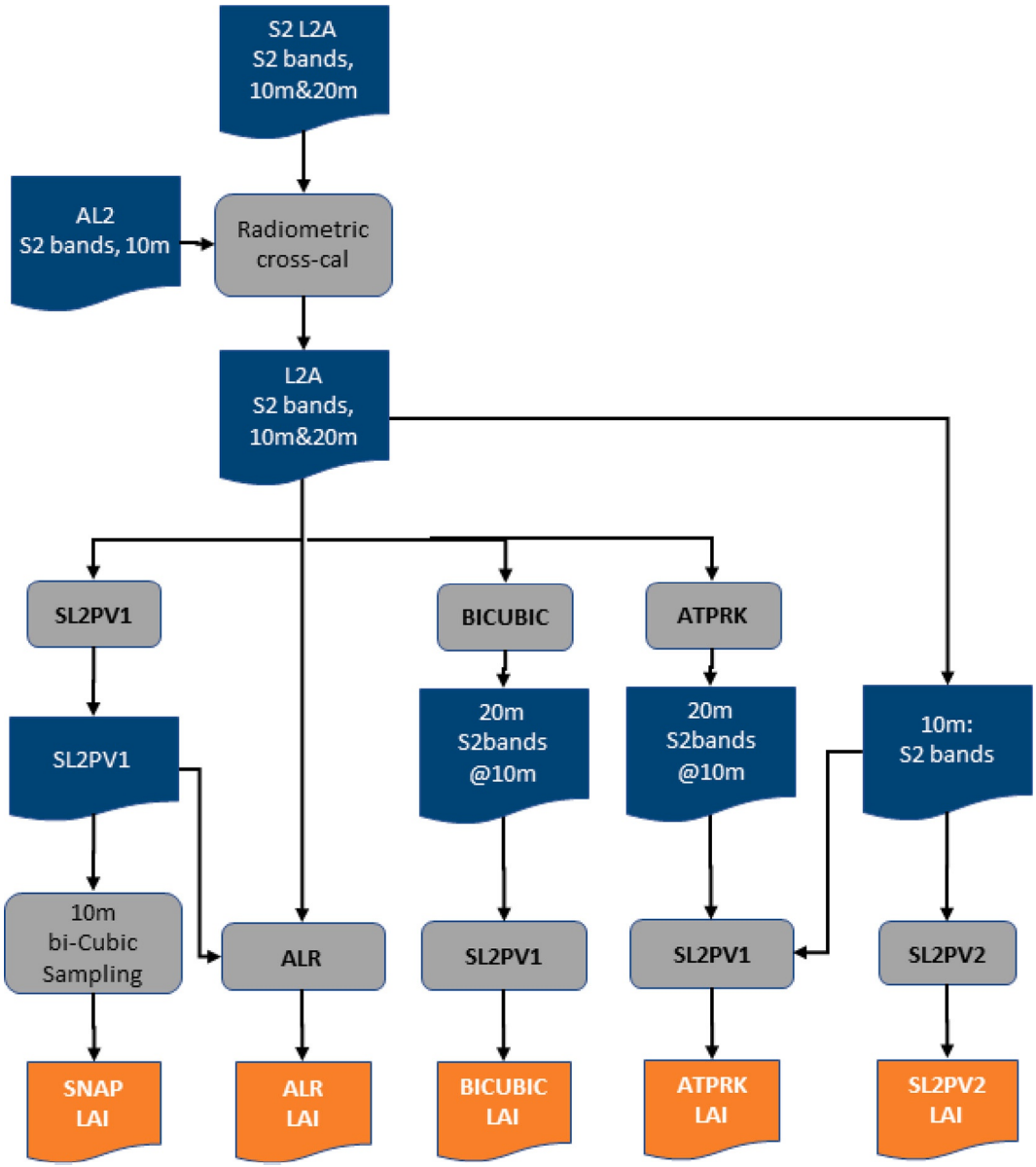


**Fig. B1.** LAI production flow chart from S2 imagery. Blue boxes indicate inputs to algorithms. Gray boxes indicate algorithms. Orange boxes indicate LAI products. (For interpretation of the references to colour in this figure legend, the reader is referred to the web version of this article.)

## Appendix C. Calibration of regressions required for SL2PV1 LAI to in-situ LAI transfer functions

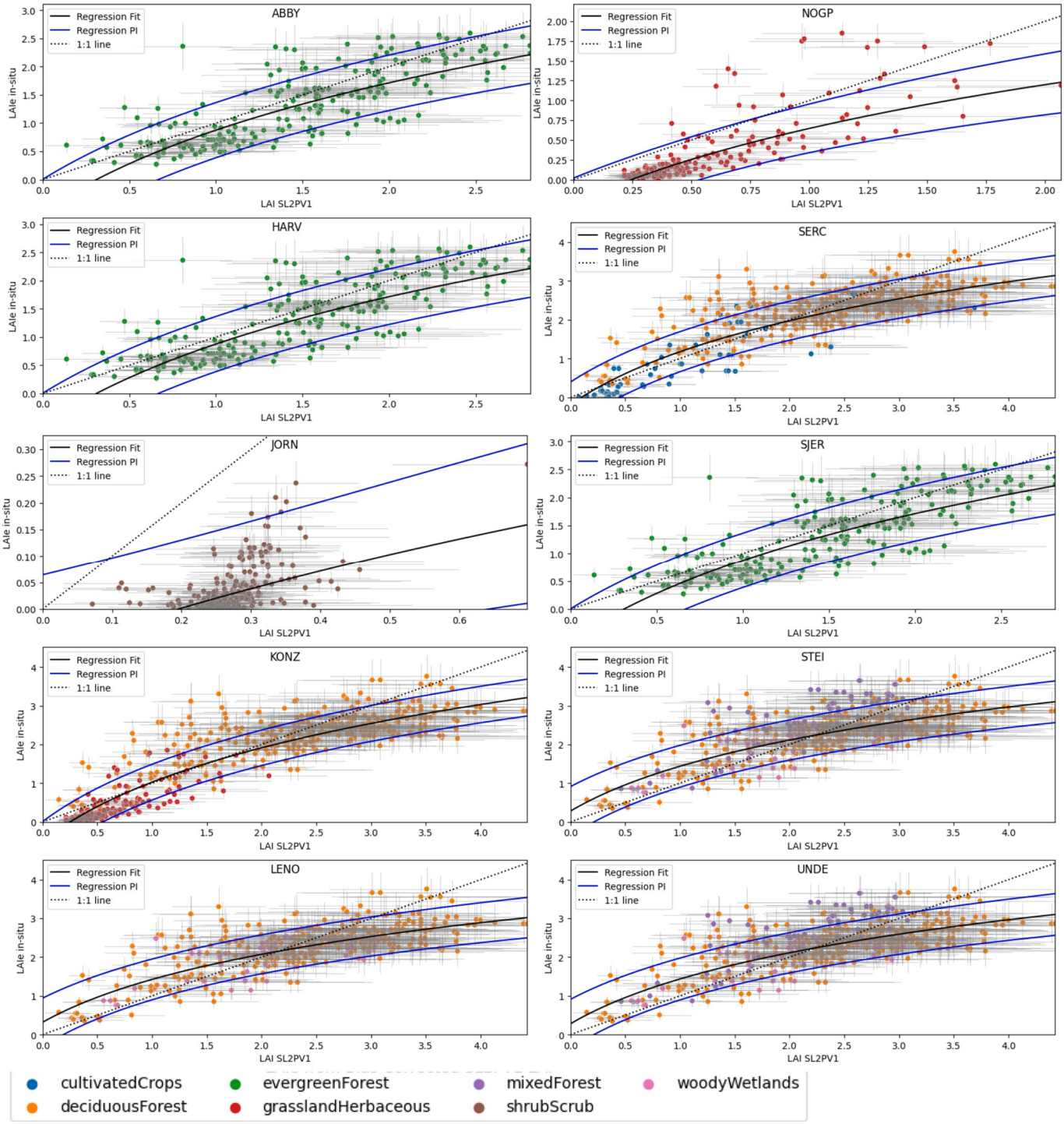


**Fig. C1.** Scatter plots of matching SL2PV1 LAI from 20 m L2 pixels and in-situ LAIe for all NEON ESUs with the same land cover as ESUs within a selected NEON site. Gray bars indicate 1 standard deviation measurement error intervals for measurements, blue lines indicate 67.5%ile prediction interval, and dotted line indicates 1:1 line. (For interpretation of the references to colour in this figure legend, the reader is referred to the web version of this article.)

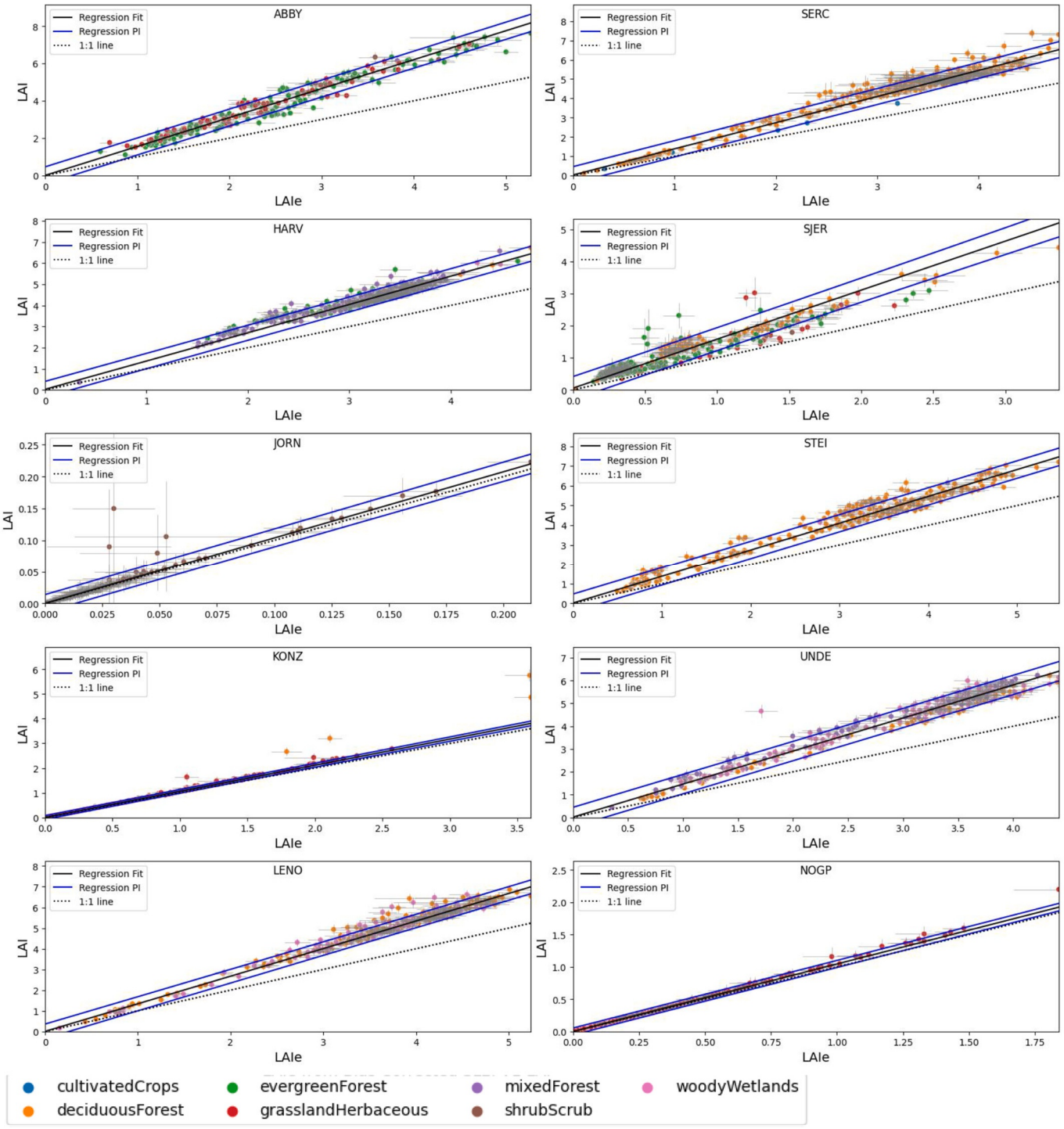


**Fig. C2.** Scatter plots of in-situ PAI versus in-situ PAIe for NEON sites together with the PAIe-PAI line fit and corresponding 16.25%ile to 83.75%ile PAI prediction intervals (blue lines). Also shown are the final Transfer Function (TF) 16.25%ile to 83.75%ile LAI prediction intervals. Gray bars indicate 1 standard deviation measurement error intervals for measurements. (For interpretation of the references to colour in this figure legend, the reader is referred to the web version of this article.)

## Appendix D. Per-pixel comparisons using L2 inputs

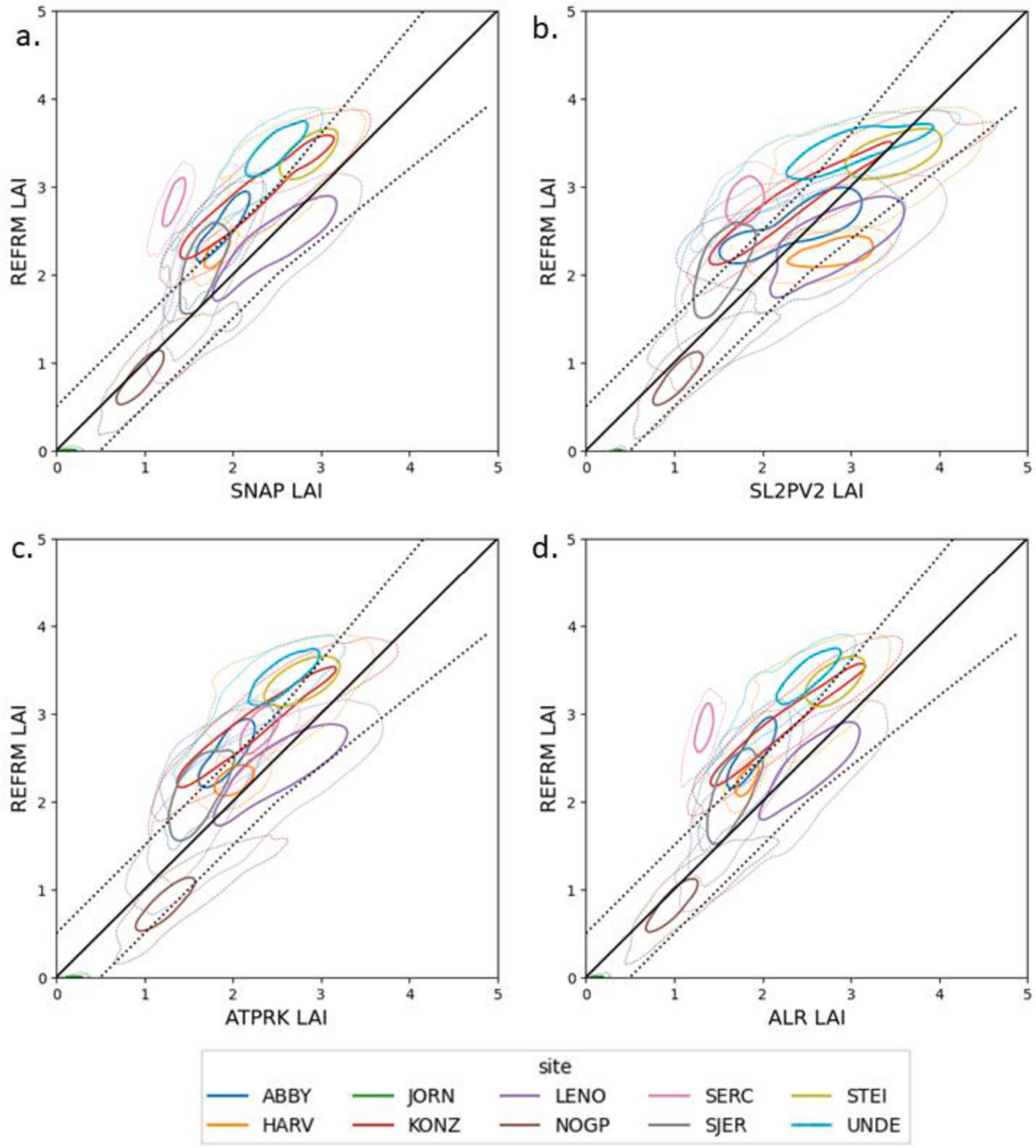


**Fig. D1.** Kernel density plots of estimated 10 m LAI from 20 m resolution L2 imagery versus reference 10 m LAI. Solid (dashed) contours correspond to 50 percentile (10 percentile) cumulative probability density. Dashed line corresponds to GCOS LAI uncertainty requirement, solid line corresponds to 1:1 lin.

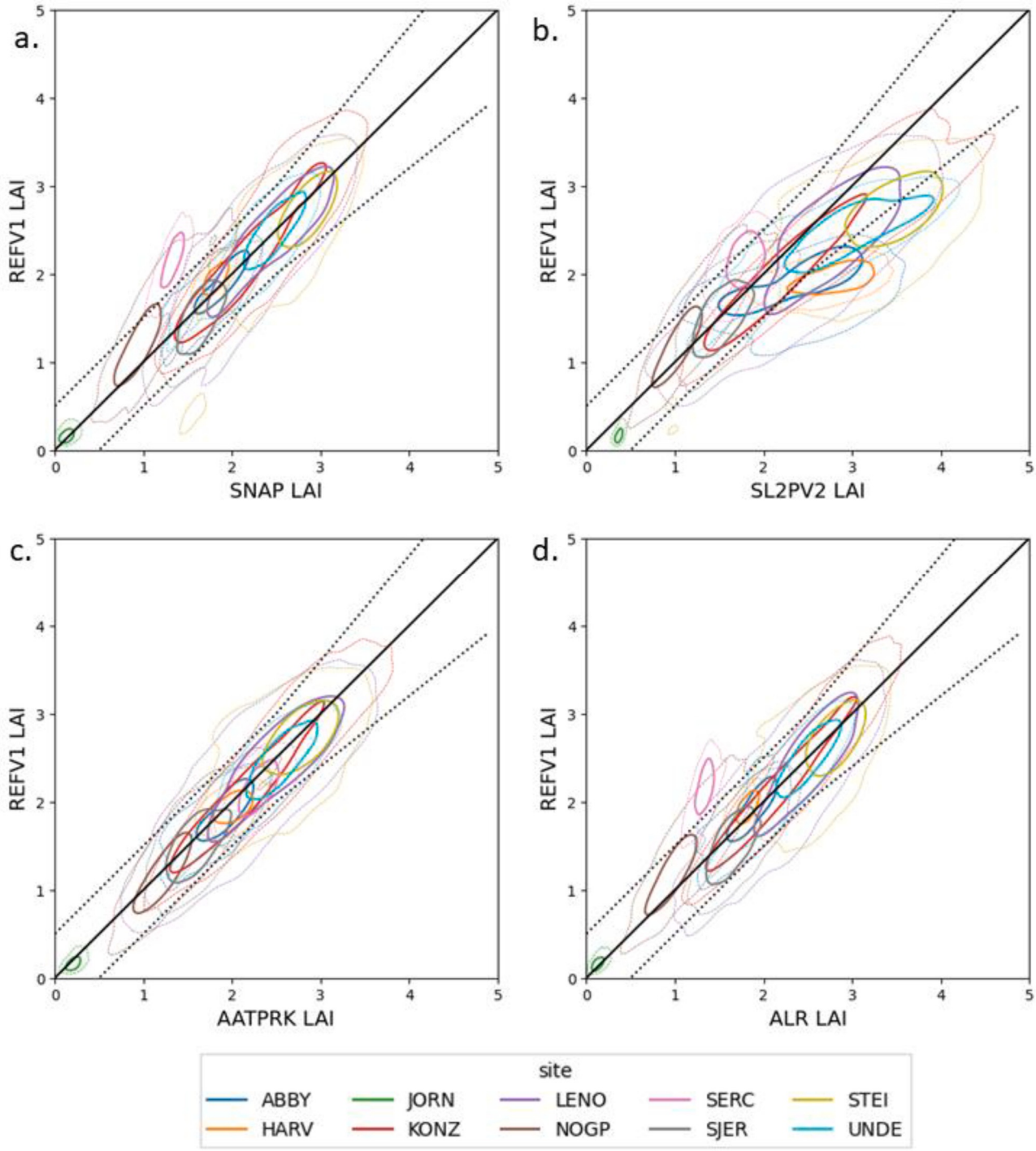


**Fig. D2.** Kernel density plots of estimated 10 m LAI from 20 m resolution L2 imagery versus 10 m LAI from SL2PV1 applied to 10 m resolution AL2 imagery for each site. Solid (dashed) contours correspond to 50 percentile (10 percentile) cumulative probability density. Dashed. line corresponds to GCOS LAI uncertainty requirement, solid line corresponds to 1:1 lin.

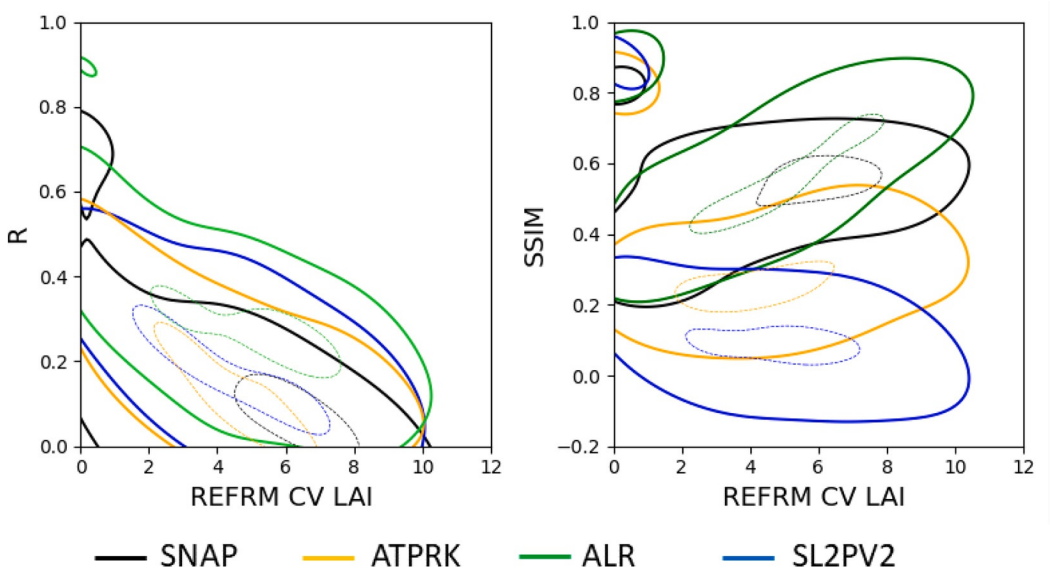


**Fig. D3.** Kernel density plots of Pearson correlation coefficient (R) (left panel) and Structural Similarity Image Metric (SSIM) right column versus reference LAI coefficient of variation (REFRM CV LAI) based on input L2 data from all sites. All samples were extracted using 110 m × 110 m moving windows. Solid (dashed) contours indicate the 83.75%ile (16.25%ile) of each distribution, bracketing the 67.5%ile central interval.

**Table D1**
Site accuracy, precision, and uncertainty in units of LAI for comparisons to REFRM reference maps. Worst corresponds to worst site. Green indicates best methods within rounding error of 0.02. Sites in bold are forested.

| Site | U | | | | A | | | | P | | | |
|---|---|---|---|---|---|---|---|---|---|---|---|---|
| | SNAP | ATPRK | ALR | SL2PV2 | SNAP | ATPRK | ALR | SL2PV2 | SNAP | ATPRK | ALR | SL2PV2 |
| Mean | 0.62 | 0.62 | 0.55 | 0.58 | -0.45 | -0.44 | -0.29 | -0.07 | 0.24 | 0.24 | 0.27 | 0.36 |
| Range | 1.32 | 1.32 | 0.66 | 0.64 | 1.65 | 1.67 | 1.35 | 1.47 | 0.29 | 0.30 | 0.33 | 0.51 |
| **ABBY** | 0.67 | 0.68 | 0.66 | 0.54 | -0.59 | -0.59 | -0.56 | -0.02 | 0.32 | 0.34 | 0.35 | 0.54 |
| **HARV** | 0.43 | 0.43 | 0.28 | 0.60 | -0.42 | -0.41 | -0.21 | 0.49 | 0.13 | 0.13 | 0.19 | 0.34 |
| JORN | 0.15 | 0.15 | 0.23 | 0.37 | 0.14 | 0.14 | 0.22 | 0.36 | 0.07 | 0.06 | 0.07 | 0.03 |
| KONZ | 0.67 | 0.65 | 0.64 | 0.52 | -0.61 | -0.61 | -0.57 | -0.30 | 0.28 | 0.22 | 0.29 | 0.43 |
| LENO | 0.38 | 0.37 | 0.43 | 0.62 | 0.14 | 0.17 | 0.16 | 0.39 | 0.36 | 0.33 | 0.40 | 0.48 |
| NOGP | 0.29 | 0.31 | 0.57 | 0.37 | 0.19 | 0.22 | 0.50 | 0.29 | 0.22 | 0.22 | 0.28 | 0.24 |
| SERC | 1.47 | 1.46 | 0.53 | 1.01 | -1.46 | -1.45 | -0.49 | -0.98 | 0.17 | 0.19 | 0.20 | 0.25 |
| **SJER** | 0.52 | 0.52 | 0.58 | 0.61 | -0.40 | -0.39 | -0.46 | -0.51 | 0.34 | 0.34 | 0.35 | 0.35 |
| **STEI** | 0.61 | 0.66 | 0.71 | 0.49 | -0.51 | -0.56 | -0.59 | 0.06 | 0.34 | 0.36 | 0.40 | 0.49 |
| **UNDE** | 0.95 | 0.96 | 0.88 | 0.69 | -0.93 | -0.94 | -0.85 | -0.53 | 0.20 | 0.20 | 0.22 | 0.44 |

**Table D2**
Site R and SSIM for comparisons to REFRM reference maps. Green indicates best methods within rounding error of 0.02. Bold sites are forested.

| Site | R | | | | SSIM | | | |
|---|---|---|---|---|---|---|---|---|
| | SNAP | ATPRK | ALR | SL2PV2 | SNAP | ATPRK | ALR | SL2PV2 |
| Mean | 0.54 | 0.59 | 0.53 | 0.50 | 0.71 | 0.73 | 0.67 | 0.62 |
| Range | 0.64 | 0.54 | 0.55 | 0.67 | 0.46 | 0.46 | 0.59 | 0.75 |
| **ABBY** | 0.53 | 0.51 | 0.44 | 0.36 | 0.73 | 0.73 | 0.69 | 0.54 |
| **HARV** | 0.42 | 0.48 | 0.35 | 0.28 | 0.86 | 0.87 | 0.76 | 0.65 |
| JORN | 0.11 | 0.34 | 0.28 | 0.27 | 0.42 | 0.42 | 0.23 | 0.11 |
| KONZ | 0.75 | 0.89 | 0.83 | 0.88 | 0.78 | 0.88 | 0.82 | 0.86 |
| LENO | 0.61 | 0.64 | 0.57 | 0.51 | 0.70 | 0.73 | 0.66 | 0.59 |
| NOGP | 0.75 | 0.79 | 0.75 | 0.79 | 0.87 | 0.88 | 0.80 | 0.86 |
| SERC | 0.54 | 0.43 | 0.47 | 0.21 | 0.65 | 0.64 | 0.77 | 0.64 |
| **SJER** | 0.59 | 0.61 | 0.54 | 0.56 | 0.59 | 0.63 | 0.60 | 0.61 |
| **STEI** | 0.53 | 0.50 | 0.45 | 0.43 | 0.73 | 0.70 | 0.63 | 0.59 |
| **UNDE** | 0.72 | 0.90 | 0.90 | 0.88 | 0.75 | 0.91 | 0.90 | 0.90 |

## Appendix E. Comparison of 10 m LAI maps from tested algorithms versus REFRM and REFV1 LAI maps

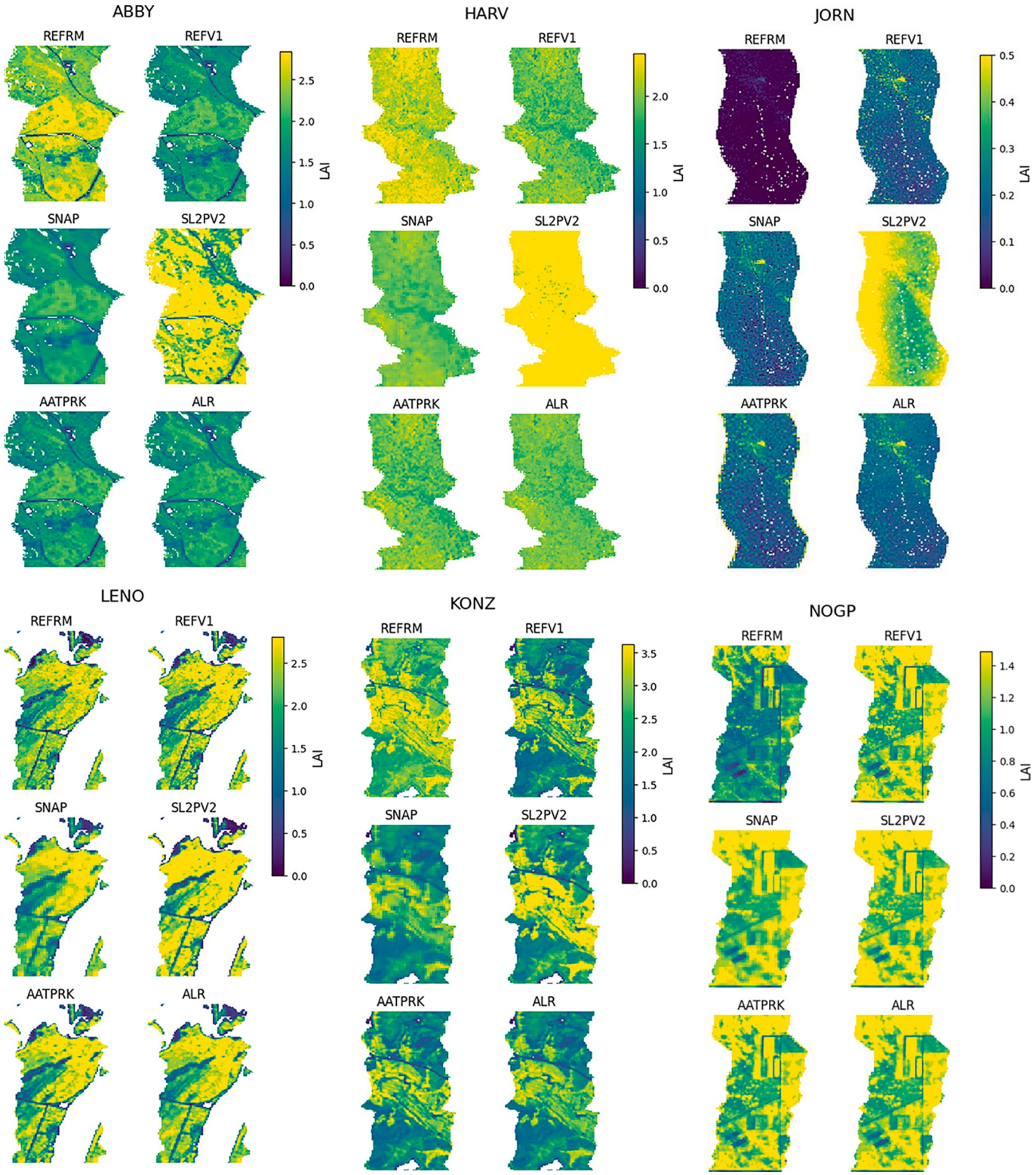


**Fig. E1.** 10 m resolution reference LAI maps based on input 10 m synthetic imagery for S2 bands (REFRM shows LAI traceable to in-situ fiducial reference measurements and REFV1 shows LAI without accounting for canopy clumping) and algorithm estimates (BSNAP, SL2PV2, ATPRK, ALR) using synthetic S2 imagery for all sites.

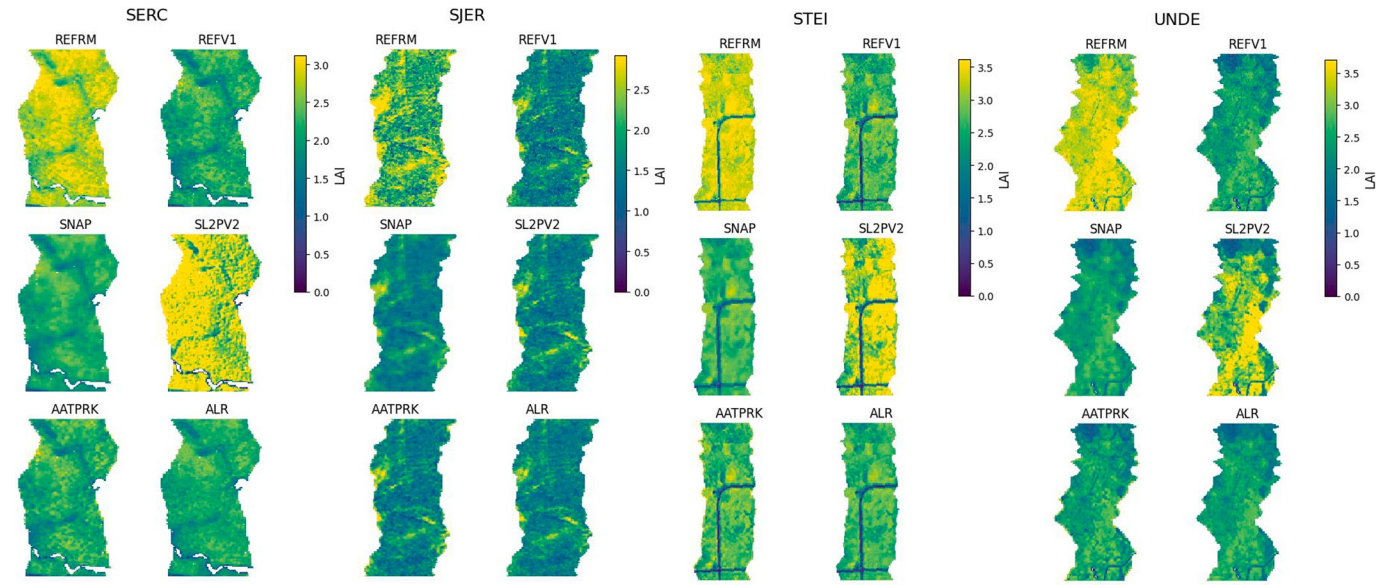


**Fig. E1.** (*continued*).

## Appendix F. LAI maps and performance metrics for BICUBIC algorithm versus ATPRK algorithm

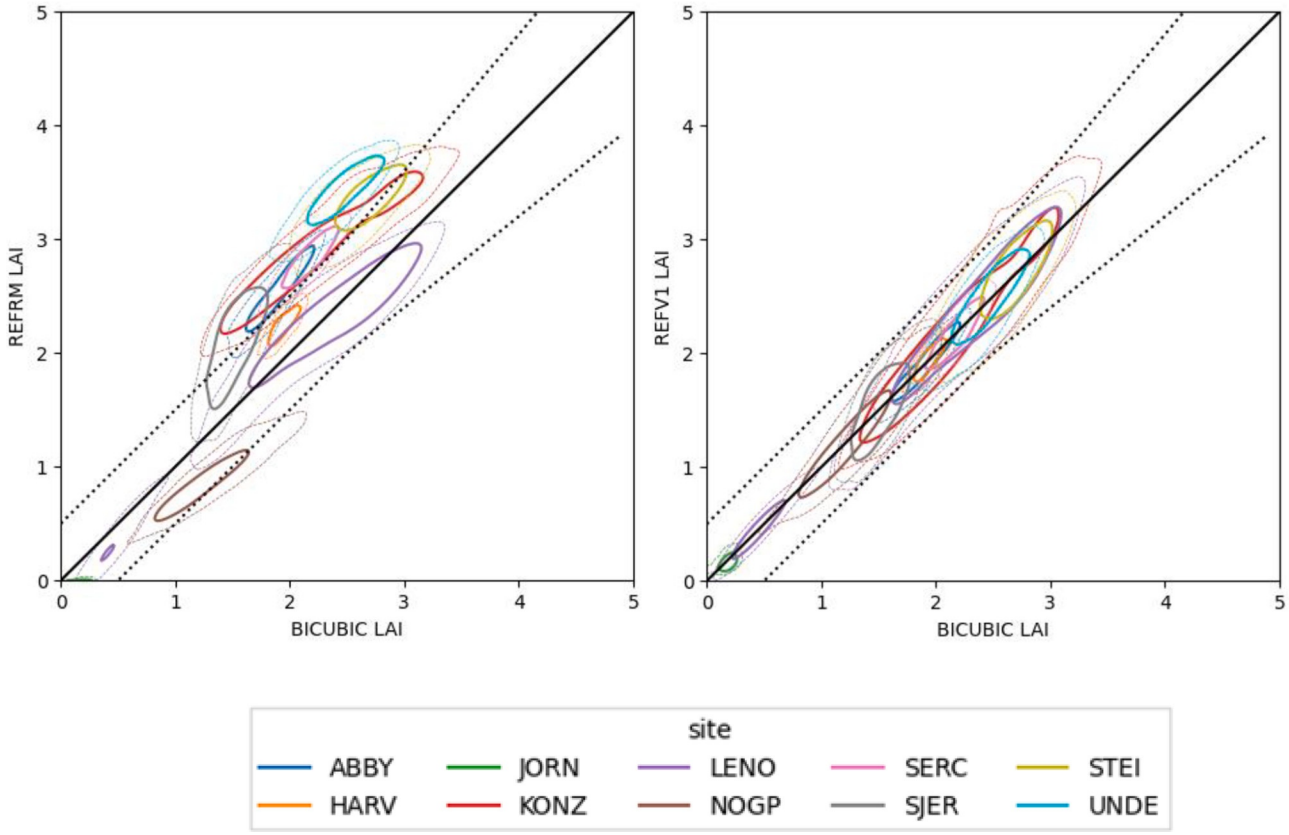


**Fig. F1.** Kernel density plots of estimated 10 m LAI from 20 m resolution AL2 imagery versus REFRM 10 m LAI (left panel;) and REFV1 10 m LAI (right panel) for each site. Solid (dashed) contours correspond to 50 percentile (10 percentile) cumulative probability density. Dashed line corresponds to GCOS LAI uncertainty requirement, solid line corresponds to 1:1 line.

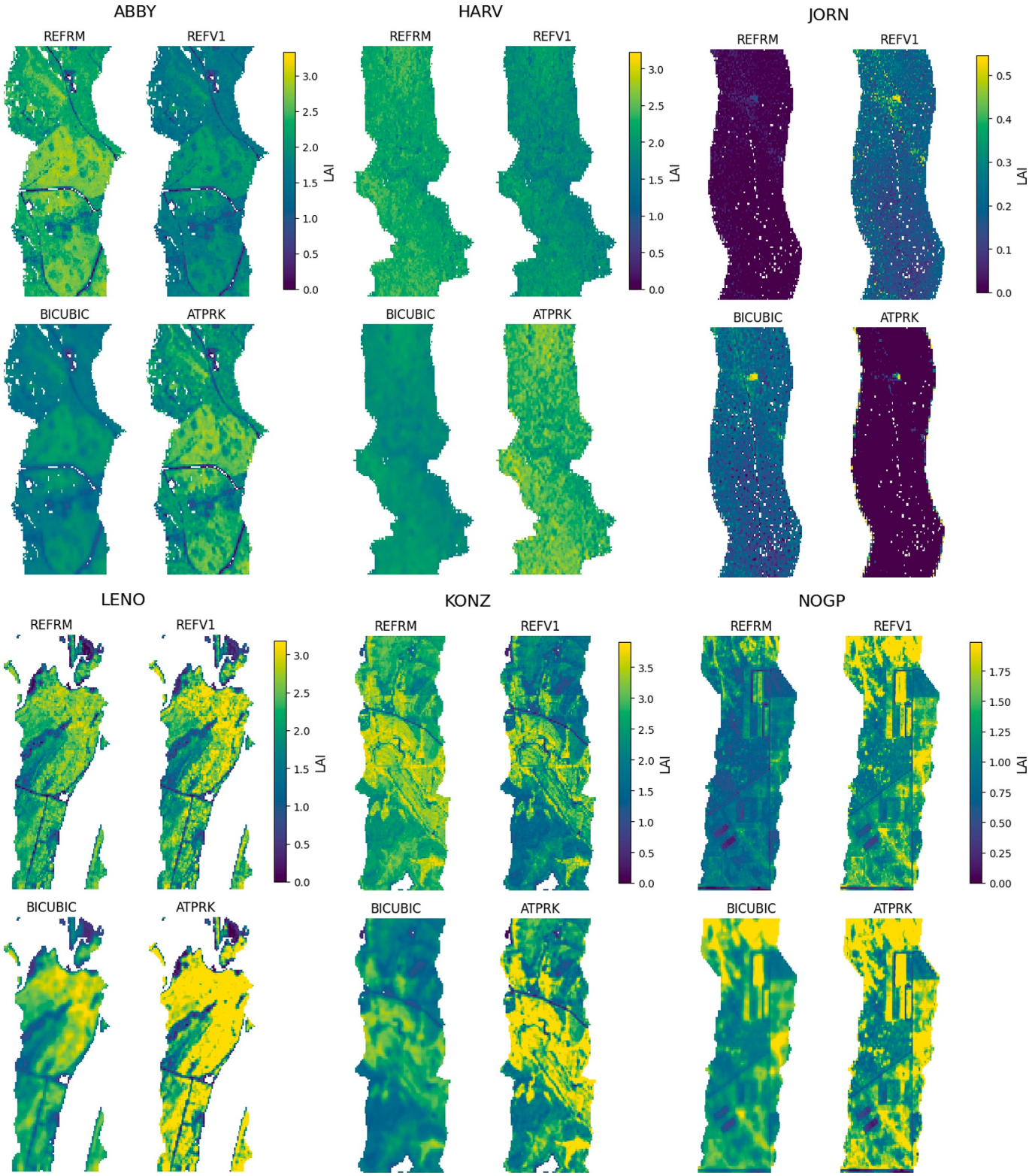


**Fig. F2.** 10 m resolution reference LAI maps based on input 10 m synthetic imagery for S2 bands (REFRM shows LAI traceable to in-situ fiducial reference measurements and REFV1 shows LAI without accounting for canopy clumping) and algorithm estimates (BICUBIC, ATPRK) using synthetic S2 imagery for all sites.

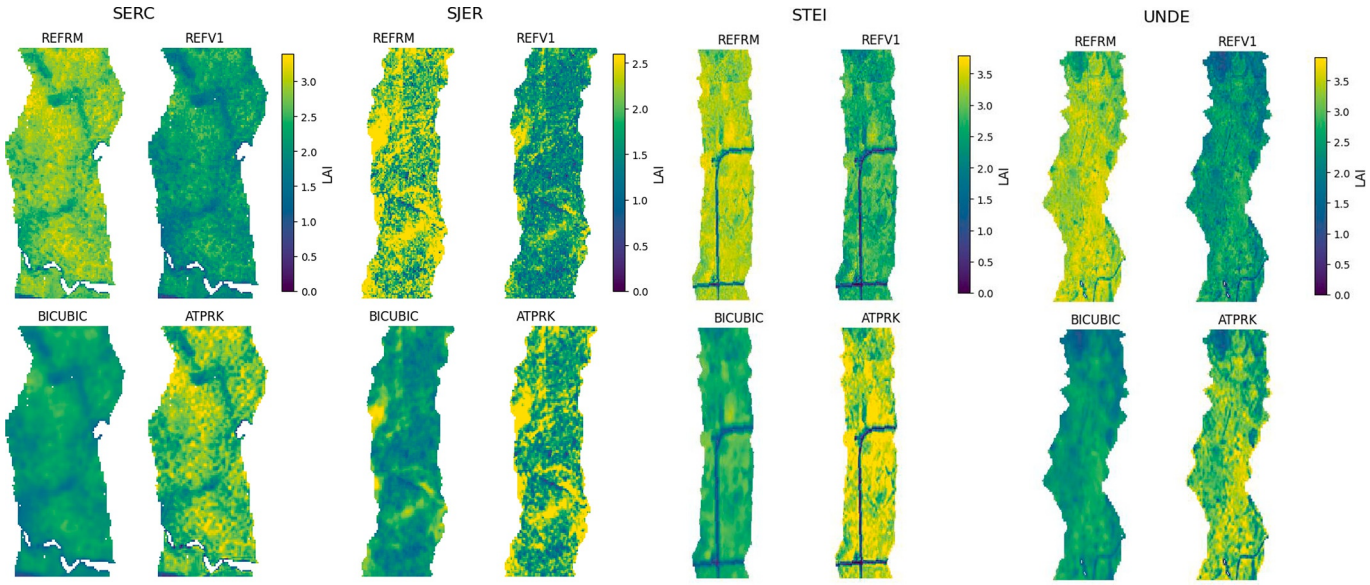


**Fig. F2.** (*continued*).

## Appendix G. Sensitivity of performance metrics to clumping uncertainty

See Tables G1–G3.

**Table G1**
Site uncertainty and accuracy, in units of LAI using 100% of the REFRM LAI as reference maps. Green indicates best methods within rounding error of 0.02. Forested sites indicated in bold.

| Site | U | | | | A | | | |
|---|---|---|---|---|---|---|---|---|
| | SNAP | ATPRK | ALR | SL2PV2 | SNAP | ATPRK | ALR | SL2PV2 |
| mean | 0.55 | 0.54 | 0.55 | 0.57 | -0.36 | -0.36 | -0.36 | 0.15 |
| range | 0.77 | 0.78 | 0.77 | 0.79 | 1.40 | 1.41 | 1.43 | 1.63 |
| **ABBY** | 0.64 | 0.63 | 0.65 | 0.56 | -0.61 | -0.62 | -0.62 | 0.28 |
| **HARV** | 0.30 | 0.30 | 0.30 | 1.18 | -0.29 | -0.29 | -0.28 | 1.11 |
| JORN | 0.19 | 0.18 | 0.20 | 0.42 | 0.17 | 0.17 | 0.19 | 0.42 |
| KONZ | 0.68 | 0.66 | 0.66 | 0.50 | -0.63 | -0.62 | -0.63 | -0.19 |
| LENO | 0.26 | 0.22 | 0.20 | 0.52 | 0.08 | 0.09 | 0.10 | 0.37 |
| NOGP | 0.50 | 0.51 | 0.53 | 0.58 | 0.46 | 0.46 | 0.48 | 0.53 |
| **SERC** | 0.66 | 0.66 | 0.67 | 0.41 | -0.65 | -0.65 | -0.66 | 0.09 |
| **SJER** | 0.62 | 0.58 | 0.57 | 0.58 | -0.54 | -0.54 | -0.52 | -0.53 |
| **STEI** | 0.71 | 0.68 | 0.72 | 0.39 | -0.67 | -0.66 | -0.70 | -0.13 |
| **UNDE** | 0.96 | 0.96 | 0.96 | 0.60 | -0.94 | -0.95 | -0.95 | -0.40 |

**Table G2**
Site uncertainty and accuracy, in units of LAI using 105% of the REFRM LAI as reference maps. Green indicates best methods within rounding error of 0.02. Forested sites indicated in bold.

| Site | U | | | | A | | | |
|---|---|---|---|---|---|---|---|---|
| | SNAP | ATPRK | ALR | SL2PV2 | SNAP | ATPRK | ALR | SL2PV2 |
| mean | 0.64 | 0.62 | 0.63 | 0.58 | -0.47 | -0.47 | -0.47 | 0.04 |
| range | 0.94 | 0.94 | 0.96 | 0.67 | 1.53 | 1.53 | 1.55 | 1.63 |
| **ABBY** | 0.76 | 0.75 | 0.77 | 0.51 | -0.73 | -0.74 | -0.74 | 0.16 |
| **HARV** | 0.41 | 0.41 | 0.41 | 1.08 | -0.40 | -0.40 | -0.40 | 1.00 |
| JORN | 0.19 | 0.18 | 0.20 | 0.42 | 0.17 | 0.17 | 0.19 | 0.42 |
| KONZ | 0.82 | 0.79 | 0.80 | 0.55 | -0.77 | -0.76 | -0.77 | -0.33 |
| LENO | 0.26 | 0.19 | 0.17 | 0.43 | -0.02 | -0.01 | 0.01 | 0.27 |
| NOGP | 0.45 | 0.47 | 0.48 | 0.54 | 0.41 | 0.41 | 0.43 | 0.48 |
| **SERC** | 0.80 | 0.80 | 0.81 | 0.41 | -0.79 | -0.79 | -0.80 | -0.05 |
| **SJER** | 0.73 | 0.69 | 0.68 | 0.68 | -0.65 | -0.64 | -0.63 | -0.63 |
| **STEI** | 0.86 | 0.84 | 0.88 | 0.46 | -0.83 | -0.82 | -0.86 | -0.29 |
| **UNDE** | 1.12 | 1.12 | 1.13 | 0.72 | -1.11 | -1.11 | -1.12 | -0.56 |

**Table G3**
Site uncertainty and accuracy, in units of LAI using 110% of the REFRM LAI as reference maps. Green indicates best methods within rounding error of 0.02. Forested sites indicated in bold.

| Site | U | | | | A | | | |
|---|---|---|---|---|---|---|---|---|
| | SNAP | ATPRK | ALR | SL2PV2 | SNAP | ATPRK | ALR | SL2PV2 |
| mean | 0.73 | 0.72 | 0.72 | 0.60 | -0.58 | -0.58 | -0.58 | -0.06 |
| range | 1.10 | 1.10 | 1.10 | 0.62 | 1.64 | 1.65 | 1.68 | 1.62 |
| **ABBY** | 0.88 | 0.88 | 0.89 | 0.49 | -0.85 | -0.86 | -0.86 | 0.03 |
| **HARV** | 0.52 | 0.52 | 0.52 | 0.98 | -0.51 | -0.51 | -0.51 | 0.88 |
| JORN | 0.19 | 0.18 | 0.19 | 0.42 | 0.17 | 0.17 | 0.19 | 0.42 |
| KONZ | 0.95 | 0.93 | 0.93 | 0.64 | -0.92 | -0.91 | -0.91 | -0.48 |
| LENO | 0.30 | 0.23 | 0.21 | 0.36 | -0.12 | -0.11 | -0.09 | 0.17 |
| NOGP | 0.41 | 0.42 | 0.43 | 0.49 | 0.37 | 0.37 | 0.39 | 0.43 |
| **SERC** | 0.94 | 0.94 | 0.95 | 0.44 | -0.93 | -0.93 | -0.94 | -0.19 |
| **SJER** | 0.83 | 0.79 | 0.78 | 0.79 | -0.75 | -0.75 | -0.73 | -0.74 |
| **STEI** | 1.02 | 1.00 | 1.04 | 0.57 | -0.99 | -0.99 | -1.02 | -0.45 |
| **UNDE** | 1.29 | 1.29 | 1.29 | 0.85 | -1.28 | -1.28 | -1.28 | -0.73 |

## References


Armannsson, S.E., Ulfarsson, M.O., Sigurdsson, J., Nguyen, H.V., Sveinsson, J.R., 2021. A comparison of optimized Sentinel-2 super-resolution methods using Wald's protocol and Bayesian optimization. Remote Sens. 13 https://doi.org/10.3390/rs13112192.

Awaya, Y., Araki, K., 2023. Estimating three-dimensional distribution of leaf area using airborne LiDAR in deciduous broad-leaved Forest. Remote Sens. 2023, 15. https://doi.org/10.3390/rs15123043.

Barnett, D.T., Duffy, P.A., Schimel, D.S., Krauss, R.E., Irvine, K.M., Davis, F.W., Gross, J. E., Azuaje, E.I., Thorpe, A.S., Gudex-Cross, D., Patterson, M., McKay, J.M., McCorkel, J.T., Meier, C.L., 2019. The terrestrial organism and biogeochemistry spatial sampling design for the National Ecological Observatory Network. Ecosphere 10, e02540. https://doi.org/10.1002/ecs2.2540.

Béland, M., Widlowski, J.-L., Fournier, R.A., Côté, J.-F., Verstraete, M.M., 2011. Estimating leaf area distribution in savanna trees from terrestrial LiDAR measurements. Agric. For. Meteorol. 151 https://doi.org/10.1016/j.agrformet.2011.05.004.

Brown, L., Courtney Meier, M., Morris, H., Pastor-Guzman, J., Bai, G., Lerebourg, C., Gobron, N., Lanconelli, C., Clerici, M., Dash, J., 2020. Evaluation of global leaf area index and fraction of absorbed photosynthetically active radiation products over North America using Copernicus ground based observations for validation data. Remote Sens. Environ. 247, 111935 https://doi.org/10.1016/j.rse.2020.111935.

Brown, L., Fernandes, R., Djamai, N., Meier, C., Gobron, N., Morris, H., Canisius, C., Bai, G., Lebourg, C., L'Antonelli, C., Clérico, M., Dash, J., 2021a. Validation of baseline and modified Sentinel-2 level 2 prototype processor leaf area index retrievals over the United States. IISPRS J. Photogramm. Remote Sens. 175, 71–87. https://doi.org/10.1016/j.isprsjprs.2021.02.020.

Brodu, N., 2017. Super-resolving multiresolution images with band-independent geometry of multispectral pixels. IEEE Trans. Geosci. Remote Sens. 55 (8), 4610–4617. https://doi.org/10.1109/TGRS.2017.2694881.

Brown, L., Camacho, F., García-Santos, V., Origo, N., Fuster, B., Morris, H., Pastor-Guzman, J., Sánchez-Sapero, J., Morrone, R., Ryder, J., Nightingale, J., Boccia, V., Dash, J., 2021b. Fiducial reference measurements for vegetation bio-geophysical variables: an end-to-end uncertainty evaluation framework. Remote Sens. 13, 3194. https://www.mdpi.com/2072-4292/13/16/3194.

Brown, L.A., Morris, H., Leblanc, S., Bai, G., Lanconelli, C., Gobron, N., Meier, C., Dash, J., 2023. HemiPy: a Python module for automated estimation of forest biophysical variables and uncertainties from digital hemispherical photographs. Methods Ecol. Evol. 00, 1–12. https://doi.org/10.1111/2041-210X.14199.

Brown, L.A., Morris, H., Morrone, R., Sinclair, M., Williams, O., Hunt, M., Bandopadhyay, S., Guo, X., Akcay, H., Dash, J., 2024. Near-infrared digital hemispherical photography enables correction of plant area index for woody material during leaf-on conditions. Eco. Inform. 79, 102441 https://doi.org/10.1016/j.ecoinf.2023.102441.

Butson, C.R., Fernandes, R.A., 2004. 2004. A consistency analysis of surface reflectance and leaf area index retrieval from overlapping clear-sky Landsat ETM+ imagery. Remote Sens. Environ. 89, 369–380.

Chen, J.M., Rich, P.M., Gower, S.T., Norman, J.M., Plummer, S., 1997. Leaf area index of boreal forests: theory, techniques, and measurements. J. Geophys. Res. 102 (D24) https://doi.org/10.1029/97JD01107.

Clerc, S., MPC Team, 2021. S2 MPC L1C Data Quality Report, European Space Agency, S2-PDGS-MPC-DQR, 64. https://sentinel.esa.int/documents/247904/685211/Sentinel-2_L1C_Data_Quality_Report.pdf/6ad66f15-48ca-4e65-b304-59ef00b7f0e0?version=4.0&t=1623227693274 accessed on October 20, 2023.

Colombo, R., 2003. Retrieval of leaf area index in different vegetation types using high resolution satellite data. Remote Sens. Environ. 86 https://doi.org/10.1016/S0034-4257(03)00094-4.

Danson, F.M., Sasse, F., Schofield, L.A., 2018. Spectral and spatial information from a novel dual-wavelength full-waveform terrestrial laser scanner for forest ecology. Interface. Focus 8 (2). https://doi.org/10.1098/rsfs.2017.0049.

Defourny, P., Bontemps, S., Bellemans, N., Cara, C., Dedieu, G., Guzzonato, E., Hagolle, O., Inglada, J., Nicola, L., Rabaute, T., Savinaud, M., Udroiu, C., Valero, S., Bégué, A., Dejoux, J.-F., El Harti, A., Ezzahar, J., Kussul, N., Labbassi, K., Lebourgeois, V., Miao, Z., Newby, T., Nyamugama, A., Salh, N., Shelestov, A., Simonneaux, V., Traore, P., Traore, S., Koetz, B., 2019. Near real-time agriculture monitoring at national scale at parcel resolution: performance assessment of the Sen2-Agri automated system in various cropping systems around the world. Remote Sens. Environ. 221 https://doi.org/10.1016/j.rse.2018.11.007.

Djamai, N., Fernandes, R., 2018. Comparison of SNAP-derived sentinel-2A L2A product to ESA product over Europe. Remote Sens. 10 https://doi.org/10.3390/rs10060926.

Djamai, N., Fernandes, R., 2021. Active learning regularization increases clear sky retrieval rates for vegetation biophysical variables using Sentinel-2 data. Remote Sens. Environ. 254 https://doi.org/10.1016/j.rse.2020.112241.

Djamai, N., Fernandes, R., Weiss, M., McNairn, H., Goïta, K., 2019. Validation of the sentinel simplified level 2 product prototype processor (SL2P) for mapping cropland biophysical variables using Sentinel-2/MSI and Landsat-8/OLI data. Remote Sens. Environ. 225, 416–430. https://doi.org/10.1016/j.rse.2019.03.020.

Dong, Y., Li, J., Jiao, Z., Liu, Q., Zhao, J., Xu, B., Zhang, H., Zhang, Z., Liu, C., Knyazikhin, Y., Myneni, R., 2023. A method for retrieving coarse-resolution leaf area index for mixed biomes using a mixed-pixel correction factor. IEEE Trans. Geosci. Remote Sens. 61 https://doi.org/10.1109/TGRS.2023.3235949.

dos Santos, L.M., Araújo e Silva Ferraz, G., de Souza Barbosa, B., Diotto, A.V., Andrade, M.T., Conti, L., Rossi, G., 2020. Determining the leaf area index and percentage of area covered by coffee crops using UAV RGB images, IEEE journal; of selected topics in applied. Earth Observ. Remote Sens. 13 https://doi.org/10.1109/JSTARS.2020.3034193.

Doxani, G., Vermote, E., Roger, J.-C., Gascon, F., Adriaensen, S., Frantz, D., Hagolle, O., Hollstein, A., Kirches, G., Li, F., Louis, J., Mangin, A., Pahlevan, N., Pflug, B., Vanhellemont, Q., 2018. Atmospheric correction inter-comparison exercise. Remote Sens. 10 https://doi.org/10.3390/rs10020352.

Dube, N., Bryant, B., Sari-Sarraf, H., Kelly, B., Martin, C.F., Deb, S., Ritchie, G.L., 2019. In situ cotton leaf area index by height using three-dimensional point clouds. Agron. J. 111, 2999–3007. https://doi.org/10.2134/agronj2019.01.0018.

ESA, 2023a. Sentinel-2 Spectral Response Functions, data repository, COPE-GSEG-EOPG-TN-15-0007, 2023. https://sentinels.copernicus.eu/web/sentinel/user-guides/sentinel-2-msi/document-library/-/asset_publisher/Wk0TKajiISaR/content/sentinel-2a-spectral-responses.

ESA, 2023b. Sentinel-2A Point Spread Function. Retrieved August 1, 2023 from. https://sentinels.copernicus.eu/documents/247904/322303/S2A_PSF.xlsx.

Estevez, J., Salinero Delgado, M., Berger, K., Pipia, Luca, Rivera Caicedo, J., Wocher, M., Reyes Muñoz, P., Tagliabue, G., Boschetti, M., Verrelst, J., 2022. Gaussian processes retrieval of crop traits in Google Earth Engine based on Sentinel-2 top-of-atmosphere data. Remote Sens. Environ. 273, 112958 https://doi.org/10.1016/j.rse.2022.112958.

Fang, H., et al., 2013. Characterization and intercomparison of global moderate resolution leaf area index (LAI) products: analysis of climatologies and theoretical uncertainties. Eur. J. Vasc. Endovasc. Surg. 118, 529–548. https://doi.org/10.1002/jgrg.20051.

Fang, H., Baret, F., Plummer, S., Schaepman-Strub, G., 2019. An overview of global leaf area index (LAI): methods, products, validation, and application. Rev. Geophys. 57 https://doi.org/10.1029/2018RG000608.

Fernandes, R., Leblanc, S.G., 2005. Parametric (modified least squares) and non-parametric (Theil–Sen) linear regressions for predicting biophysical parameters in the presence of measurement errors. Remote Sens. Environ. 95, 303–316.

Fernandes, R., Butson, C., Leblanc, S., Latifovic, R., 2003. Landsat-5 TM and Landsat-7 ETM+ based accuracy assessment of leaf area index products for Canada derived from SPOT-4 VEGETATION data. Can. J. Remote. Sens. 29 https://doi.org/10.5589/m02-092.

Fernandes, R., Plummer, S., Nightingale, J., Baret, F., Camacho, F., Fang, H., Garrigues, S., Gobron, N., Lang, M., Lacaze, R., Leblanc, S., Meroni, M., Martinez, B., Nilson, T., Pinty, B., Pisek, J., Sonnentag, O., Verger, A., Welles, J., Weiss, M., Widlowski, J.L., Schaepman-Strub, G., Roman, M., Nickeson, J., 2014. Global leaf area index product validation good practices. In: Fernandes, R., Plummer, S., Nightingale, J. (Eds.), Best Practice for Satellite-Derived Land Product Validation. Land Product Validation Subgroup (Committee on Earth Observation Satellites Working Group on Calibration and Validation). https://doi.org/10.5067/doc/ceoswgcv/lpv/lai.002.

Fernandes, R., et al., 2021. LEAF Toolbox. Canada Centre for Remote Sensing, [Computer software]. https://doi.org/10.5281/zenodo.4321298. Retrieved August 23, 2023, from. https://github.com/rfernand387/LEAF-Toolbox/wiki.

Fernandes, R., Brown, L., Canisius, F., Dash, J., He, L., Hong, G., Huang, L., Le, N.Q., MacDougall, C., Meier, C., Darko, P.O., Shah, H., Spafford, L., Sun, L., 2023. Validation of simplified level 2 prototype processor Sentinel-2 fraction of canopy cover, fraction of absorbed photosynthetically active radiation and leaf area index products over North American forests. Remote Sens. Environ. 293 https://doi.org/10.1016/j.rse.2023.113600.

Fernandes, R., Canisius, F., Harvey, K., Hong, G., MacDougall, C., Shah, H., Sun, L., 2024a. Evidence of a bias-variance trade off when correcting for bias in sentinel 2 forest LAI retrievals using radiative transfer models. Remote Sens. Environ. 305 https://doi.org/10.1016/j.rse.2024.114060.

Fernandes, R., Hong, G., Kalimpalli, S., 2024b. 10m resolution leaf area index maps for selected National Ecological Observatory Network sites traceable to fiducial reference measurements. Earth Syst. Sci. Data (in review).

Ganguly, S., Nemani, R.R., Zhang, G., Hashimoto, H., Milesi, C., Michaelis, A., Wang, W., Votava, P., Samanta, A., Melton, F., Dungan, J.L., Vermote, E., Gao, F., Knyazikhin, Y., Myneni, R.B., 2012. Generating global leaf area index from Landsat: algorithm formulation and demonstration. Remote Sens. Environ. 122 https://doi.org/10.1016/j.rse.2011.10.032.

Garrigues, S., Allard, D., Baret, F., Weiss, M., 2006. Influence of landscape spatial heterogeneity on the non-linear estimation of leaf area index from moderate spatial resolution remote sensing data. Remote Sens. Environ. 105, 286–298.

Gascon, F., Bouzinac, C., Thépaut, O., Jung, M., Francesconi, B.J., Lonjou, V., Lafrance, B., Massera, S., Gaudel-Vacaresse, A., et al., 2017. Copernicus sentinel-2A calibration and products validation status. Remote Sens. 9 (6), 584. https://doi.org/10.3390/rs9060584.

GDAL/OGR contributors, 2024. GDAL/OGR Geospatial Data Abstraction Software Library. Open Source Geospatial Foundation. https://gdal.org. https://doi.org/10.5281/zenodo.5884351.

Gebbers, R., Ehlert, D., Adamek, R., 2011. Rapid mapping of the leaf area index in agricultural crops. Agron. J. 103 https://doi.org/10.2134/agronj2011.0201.

Hosoi, F., Omasa, K., 2006. Voxel-based 3-D modeling of individual trees for estimating leaf area density using high-resolution portable scanning Lidar. IEEE Trans. Geosci. Remote Sens. 44 https://doi.org/10.1109/TGRS.2006.881743.

Houborg, R., McCabe, M.F., 2018. Daily retrieval of NDVI and LAI at 3 m resolution via the fusion of CubeSat, Landsat, and MODIS data. Remote Sens. 10 (6), 890. https://doi.org/10.3390/rs10060890.

Jin, Z., Tian, Q.C., Chen, J.M., Chen, M., 2007. Spatial scaling between leaf area index maps of different resolutions. J. Environ. Manag. 2007, 628–637.

Kamoske, A.G., Dahlin, K.M., Stark, S.C., Serbin, S.P., 2018. Leaf area density from airborne LiDAR: comparing sensors and resolutions in a temperate broadleaf forest ecosystem. For. Ecol. Manag. 433 https://doi.org/10.1016/j.foreco.2018.11.017.

Kampe, T., Gallery, W., 2015. NEON Imaging Spectrometer Geolocation Algorithm Theoretical Basis Document. NEON.DOC.001290 revision 8. https://data.neonscience.org/documents/10179/11204/NEON.DOC.001290vC/bd4dd715-53c3-4e66-bf81-3e6cfe218654?version=1.1 accessed on August 28, 2023.

Kang, Y., Ozdogan, M., Gao, F., Anderson, M.C., White, W.A., Yang, Yun, Yang, Yang, Erickson, T.A., 2021. A data-driven approach to estimate leaf area index for Landsat images over the contiguous US. Remote Sens. Environ. 258 https://doi.org/10.1016/j.rse.2021.112383.

Kganyago, M., Mhangara, P., Alexandridis, T., Laneve, G., Ovakoglou, G., Mashiyi, N., 2020. Validation of sentinel-2 leaf area index (LAI) product derived from SNAP toolbox and its comparison with global LAI products in an African semi-arid agricultural landscape. Remote Sens. Lett. 11 (10), 883–892. https://doi.org/10.1080/2150704X.2020.1767823.

Kimm, H., Guan, H., Jiang, C., Peng, B., Gentry, L., Wilkin, S., Wang, S., Cai, Y., Bernacchi, C., Peng, J., Luo, Y., 2020. Deriving high-spatiotemporal-resolution leaf area index for agroecosystems in the U.S. Corn Belt using planet labs CubeSat and STAIR fusion data. Remote Sens. Environ. 239 https://doi.org/10.1016/j.rse.2019.111615.

Kross, A., McNairn, H., Lapen, D., Sunohara, M., Champagne, C., 2015. Assessment of RapidEye vegetation indices for estimation of leaf area index and biomass in corn and soybean crops. Int. J. Appl. Earth Obs. Geoinf. 34 https://doi.org/10.1016/j.jag.2014.08.002.

Lanaras, C., Bioucas-Dias, J., Galliani, S., Baltsavias, E., 2024. SchindlerSuper-resolution of Sentinel-2 images: Learning a globally applicable deep neural network. ISPRS J. Photogramm. Remote Sens. 146 https://doi.org/10.1016/j.isprsjprs.2018.09.018.

Lang, A.R.G., Xiang, L., 1986. Estimation of leaf area index from transmission of direct sunlight in discontinuous canopies. Agric. For. Meteorol. 37 https://doi.org/10.1016/0168-1923(86)90033-x.

Law, B.E., Van Tuyl, S., Cescatti, A., Baldocchi, D.D., 2021. Estimation of leaf area index in open-canopy ponderosa pine forests at different successional stages and management regimes in Oregon. Agric. For. Meteorol. 108 https://doi.org/10.1016/S0168-1923(01)00226-X.

Lefsky, M.A., Cohen, W.B., Parker, G.G., Harding, D.J., 2002. Lidar Remote Sensing for Ecosystem Studies: Lidar, an emerging remote sensing technology that directly measures the three-dimensional distribution of plant canopies, can accurately estimate vegetation structural attributes and should be of particular interest to forest, landscape, and global ecologists. BioScience 52 (1), 19–30. https://doi.org/10.1641/0006-3568(2002)052[0019:LRSFES]2.0.CO;2.

Lupardus, R., McIntosh, A., Janz, A., Farr, D., 2019. Succession after reclamation: identifying and assessing ecological indicators of forest recovery on reclaimed oil and natural gas well pads. Ecol. Indic. 106, 105515 https://doi.org/10.1016/j.ecolind.2019.105515.

Mathworks, 2023. Piecewise Cubic Hermite Interpolating Polynomial (PCHIP). [Computer software]. Retrieved August 1, 2023, from. https://www.mathworks.com/help/matlab/ref/pchip.html.

McCabe, M.F., Aragon, B., Houborg, R., Mascaro, J., 2017. CubeSats in hydrology: ultrahigh-resolution insights into vegetation dynamics and terrestrial evaporation. Water Resour. Res. 53, 10017–10024. https://doi.org/10.1002/2017WR022240.

Mendes dos Santos, L., Araújo e Silva, G., de Souza, B., Diotto, A., Andrade, M., Conti, L., Rossi, G., 2020. Determining the leaf area index and percentage of area covered by coffee crops using UAV RGB images. IEEE J. Selected Topics Appl. Earth Observ. Remote Sensi. 13 https://doi.org/10.1109/JSTARS.2020.3034193.

Mulla, D.J., 2013. Twenty five years of remote sensing in precision agriculture: key advances and remaining knowledge gaps. Biosyst. Eng. 114, 358–371.

Müller-Wilm, U., 2018. Sen2Cor Configuration and User Manual, 2nd ed. CS, Toulouse, France.

NEON (National Ecological Observatory Network), 2023a. Spectrometer orthorectified surface directional reflectance - flightline (DP1.30006.001), RELEASE-2023a. https://doi.org/10.48443/ypjz-et36. Dataset accessed from https://data.neonscience.org on October 23, 2023.

NEON (National Ecological Observatory Network), 2023b. Spectrometer orthorectified at-sensor radiance - flightline (DP1.30008.001), RELEASE-2023b. https://doi.org/10.48443/ehnm-xd88. Dataset accessed from https://data.neonscience.org on October 23, 2023.

NEON (National Ecological Observatory Network), 2023c. Digital Hemispheric Photos of Plot Vegetation (DP1.10017.001), RELEASE-2023. https://doi.org/10.48443/t8a4-vk69. Dataset accessed from https://data.neonscience.org/data-products/DP1.10017.001/RELEASE-2023 on November 17, 2023.

Park, N.-W., Kim, Y., Kwok, G.-H., 2019. An overview of theoretical and practical issues in spatial downscaling of coarse resolution satellite-derived products. Korean J. Remote Sens. 35 https://doi.org/10.7780/kjrs.2019.35.4.8.

Schowengerdt, R., 2012. Remote Sensing: Models and Methods for Image Processing, 2nd edition. © Academic Press, p. 522.

Soudani, K., Francois, C., le Maire, G., le Dantec, V., Dufresne, E., 2006. Comparative analysis of IKONOS, SPOT, and ETM+ data for leaf area index estimation in temperate coniferous and deciduous forest stands. Remote Sens. Environ. 102, 167–175.

Sumnall, M.J., Trlica, A., Carter, D.R., Cook, R.L., Schulteampoe, O.C., Rubilar, R.A., Wynne, R.H., Thomas, V.A., 2021. Estimating the overstory and understory vertical extents and their leaf area index in intensively managed loblolly pine (*Pinus taeda* L.) plantations using airborne laser scanning. Remote Sens. Environ. 254 https://doi.org/10.1016/j.rse.2020.112250.

Tian, Y., Wang, Y., Zhang, Y., Knyazikhin, Y., Bogaert, J., Myneni, R.B., 2001. Radiative transfer based scaling of LAI retrievals from reflectance data of different resolutions. Remote Sens. Environ. 84 https://doi.org/10.1016/S0034-4257(02)00102-5.

Tran, T.D.-B., Puissant, A., Badariotti, D., Weber, C., 2011. Optimizing spatial resolution of imagery for urban form detection—the cases of France and Vietnam. Remote Sens. 3, 2128–2147.

Van der Walt, S., Schonberger, J.L., Nunez-Iglesias, J., Boulogne, F., Warner, J.D., Yager, N., et al., 2014. Scikit-image: image processing in Python. PeerJ 2, e453.

Verger, A., Baret, F., Camacho, F., 2011. Optimal modalities for radiative transfer-neural network estimation of canopy biophysical characteristics: evaluation over an agricultural area with CHRIS/PROBA observations. Remote Sens. Environ. 115, 415–426.

Verhoef, W., 1984. Light scattering by leaf layers with application to canopy reflectance modeling: the SAIL model. Remote Sens. Environ. 16 https://doi.org/10.1016/0034-4257(84)90057-9.

Wang, Z., Bovik, A.C., Sheikh, H.R., Simoncelli, E.P., 2004. Image quality assessment: from error visibility to structural similarity. IEEE Trans. Image Process. 13 (4), 600–612. https://doi.org/10.1109/TIP.2003.819861.

Wang, Q., Shi, W., Atkinson, P.M., 2016a. Area-to-point regression kriging for pan-sharpening. ISPRS J. Photogramm. Remote Sens. 114, 151–165.

Wang, Q., Shi, W., Li, Z., Atkinson, P.M., 2016b. Fusion of Sentinel-2 images. Remote Sens. Environ. 187, 241–252.

Weiss, M., Baret, F., 2016. S2ToolBox Level 2 Products: LAI, FAPAR, FCOVER, 1.0. Ed. Institut National de la Recherche Agronomique, Avignon, France. https://step.esa.int/docs/extra/ATBD_S2ToolBox_L2B_V1.0.pdf.

Weiss, M., Baret, F., 2020. S2ToolBox Level 2 Products: LAI, FAPAR, FCOVER, 2.0. Ed. Institut National de la Recherche Agronomique, Avignon, France. https://step.esa.int/docs/extra/ATBD_S2ToolBox_L2B_V2.0.pdf.

Weiss, M., Baret, F., Smith, G.J., Jonckheere, I., Coppin, P., 2004. Review of methods for in situ leaf area index (LAI) determination: Part II. Estimation of LAI, errors and sampling. Agric. For. Meteorol. 121 https://doi.org/10.1016/j.agrformet.2003.08.001.

WMO, 2022. The 2022 GCOS ECV Requirements, GCOS- No. 245, © World Meteorological Organization, p. 261.

Xu, F., Somers, B., 2021. Unmixing-based Sentinel-2 downscaling for urban land cover mapping. ISPRS J. Photogramm. Remote Sens. 171, 133–154.

Xu, B., Li, Y., Park, T., Liu, Q., Zeng, Y., Yin, Y., Yan, K., Chen, C., Zhao, J., Fan, W., Knyazikhin, Y., Myneni, R.B., 2020. Improving leaf area index retrieval over heterogeneous surface mixed with water. Remote Sens. Environ. 240 https://doi.org/10.1016/j.rse.2020.111700.

Yamazaki, D., Ikeshima, D., Tawatari, R., Yamaguchi, T., O'Loughlin, F., Neal, J.C., Sampson, C.C., Kanae, S., Bates, P.D., 2017. A high accuracy map of global terrain elevations. Geophys. Res. Lett. 44 https://doi.org/10.1002/2017GL072874.

Yang, C., Everitt, J.H., Bradford, J.M., 2009. Evaluating high resolution SPOT 5 satellite imagery for crop yield estimation. Precis. Agric. 10 (4), 292–303.

Zheng, H., Du, P., Chen, J., Xia, J., Li, E., Xu, Z., Li, X., Yokoya, N., 2017. Performance evaluation of downscaling Sentinel-2 imagery for land use and land cover classification by spectral-spatial features. Remote Sens. 9 (12), 1274. https://doi.org/10.3390/rs9121274.